2015

Experimental Investigation of Wall Shear Stress Modifications due to Turbulent Flow over an Ablative Thermal Protection System Analog Surface

Jacob Helvey
University of Kentucky, jphelv2@g.uky.edu

STUDENT AGREEMENT:

I represent that my thesis or dissertation and abstract are my original work. Proper attribution has been given to all outside sources. I understand that I am solely responsible for obtaining any needed copyright permissions. I have obtained needed written permission statement(s) from the owner(s) of each third-party copyrighted matter to be included in my work, allowing electronic distribution (if such use is not permitted by the fair use doctrine) which will be submitted to UKnowledge as Additional File.

I hereby grant to The University of Kentucky and its agents the irrevocable, non-exclusive, and royalty-free license to archive and make accessible my work in whole or in part in all forms of media, now or hereafter known. I agree that the document mentioned above may be made available immediately for worldwide access unless an embargo applies.

I retain all other ownership rights to the copyright of my work. I also retain the right to use in future works (such as articles or books) all or part of my work. I understand that I am free to register the copyright to my work.

REVIEW, APPROVAL AND ACCEPTANCE

The document mentioned above has been reviewed and accepted by the student's advisor, on behalf of the advisory committee, and by the Director of Graduate Studies (DGS), on behalf of the program; we verify that this is the final, approved version of the student's thesis including all changes required by the advisory committee. The undersigned agree to abide by the statements above.

Jacob Helvey, Student

Dr. Sean Bailey, Major Professor

Dr. James McDonough, Director of Graduate Studies

Experimental Investigation of Wall Shear Stress Modifications due to Turbulent Flow over an Ablative Thermal Protection System Analog Surface

---

THESIS

A thesis submitted in partial fulfillment of the
requirements for the degree of Master of Science in
Mechanical Engineering in the College of Engineering
at the University of Kentucky

by

Jacob Preston Helvey

Lexington, Kentucky

Director: Dr. Sean Bailey, Professor of Mechanical Engineering

Lexington, Kentucky

2015

ABSTRACT OF THESIS

Experimental Investigation of Wall Shear Stress Modifications due to Turbulent Flow over an Ablative Thermal Protection System Analog Surface

Modifications were made to the turbulent channel flow facility to allow for fully developed rough quasi-2D Poiseuille flow with flow injection through one surface and flow suction through the opposing surface. The combination of roughness and flow injection is designed to be analogous to the flow field over a thermal protection system which produces ablative pyrolysis gases during ablation. It was found that the additional momentum through the surface acted to reduce skin friction to a point below smooth-wall behavior. This effect was less significant with increasing Reynolds number. It was also found that the momentum injection modified the wake region of the flow.

KEYWORDS: Turbulence, Flow Injection, Surface Roughness, Ablative Thermal Protection Systems, Channel Flows userkeywords

Jacob Preston Helvey
July 17, 2015

Experimental Investigation of Wall Shear Stress Modifications due to Turbulent Flow over an Ablative Thermal Protection System Analog Surface

by

Jacob Preston Helvey

Dr. Sean Bailey

Director of Thesis

Dr. James M. McDonough,

Director of Graduate Studies

July 17, 2015

Acknowledgments

First and foremost, I would like to thank my advisor, Dr. Bailey, who provided me with unceasing guidance and support throughout my time as a graduate student. He has allowed me the opportunity, resources, and time to develop my engineering skills to where they are today. More than anything he has taught me to learn how to teach myself, which I believe is the most important lesson for any student so that they can bring their abilities to greater levels in the future.

The machine shop staff including Floyd Taylor and Herb Mefford were crucial to the success of this work. They provided their unique fabricating insights to help develop the modifications needed to conduct the experiment. Without their help, this work would not have been possible. Also my lab mates, without which my time as a graduate student would have been very stressful had they not been there for support.

I would also like to thank the group responsible for financially supporting this work, that being the NASA EPSCoR award (grant number NNX10AV39A).

Table of Contents

List of Figures

List of Tables

Nomenclature

Re	Reynolds number
L	Characteristic length
ν	Kinematic viscosity
$\vec{U}$	Velocity vector
U	Streamwise velocity
V	Wall-normal velocity
W	Spanwise velocity
x	Streamwise direction
y	Wall-normal direction
z	Spanwise direction
$\overline{\vec{U}}$	Time independent mean velocity vector
$\overline{U}$	Mean streamwise velocity
$\overline{V}$	Mean wall-normal velocity
$\overline{W}$	Mean spanwise velocity
$\vec{u'}$	Fluctuating velocity vector
u'	Fluctuating streamwise component of velocity
v'	Fluctuating wall-normal component of velocity
w'	Fluctuating spanwise component of velocity
t	Time
$\vec{P}$	Pressure vector divided by constant density
$\vec{F_B}$	Body forces divided by constant density
τ_ω	Wall shear stress
U_τ	Friction velocity
ρ	Fluid density
δ_ν	Viscous length

h	Channel half-height
U_b	Area-averaged streamwise velocity
κ	von Kármán constant
y^+	Wall-normal direction scaled with viscous units
U^+	Mean streamwise velocity scaled with viscous units
B	Integration constant
b	Width of channel
H	Height of channel
R	Pipe radius
Re_τ	Friction Reynolds number
$\langle U \rangle$	Average streamwise velocity
c_f	Coefficient of friction
$U_c l$	Streamwise centerline velocity
k	Roughness element height
k^+	Roughness Reynolds number
k_{rms}	Rms roughness height
f	Friction factor
D	Pipe diameter
Δp	Pressure drop over axial distance
r	Axial distance
y_o	Zero-plane displacement
Y	Wall-normal location minus zero-plane displacement
Y^+	Wall-normal location minus zero-plane displacement scaled with viscous units
h_i	Set of length scales used to characterize surface roughness
C	Integration term as a function of roughness length scales
$W(Y/h)$	Wake function
ΔU^+	Roughness function

k_s	Equivalent sand-grain roughness
k_s^+	Sand-grain roughness Reynolds number
U_{inj}^+	Injection velocity scaled with viscous units
l	Mixing length
Δs	Film thickness difference
λ	Wavelength of light
α	Observer viewing angle
n	Refractive index of oil
A_c	Cross-sectional area of pipe
d	Outer diameter of Preston tube
ΔP	Mean pressure difference between Preston tube and static pressure from wall tap
V_o	Flow injection velocity
p_w	Pressure at the rough wall
y_{τ_0}	Wall-normal location of zero shear stress
BR	Blowing ratio
U_m	Maximum measured streamwise velocity
Q	Flow rate
K	System resistance constant
U_1	Velocity at PVC inlet
A_1	Area of PVC inlet
A_2	Area of rough surface section at exit of blowing rig
c	Correction factor
ΔV	Voltage difference
U_{center}	Measured velocity by Pitot-static tube inside PVC inlet
S	Pressure transducer span
c_τ	Normalized shear stress

Chapter 1 Introduction

1.1 Introduction

In the realm of fluid mechanics, turbulence has always been an incomplete area of research in that there is currently no physical model or theory which fully explains turbulent behavior. The seemingly random fluctuations inherent to turbulent flow have been a continuing source of difficulty to defying even proper description. The Navier-Stokes equations hold the key to predicting the physics behind turbulence, however the models used to solve these non-linear equations are still in their infancy. This is due to the vast computing power required to fully resolve from the largest to the smallest physical and temporal scales of the turbulent structures. While there is currently no complete definition of turbulence, we can describe some of its characteristics in that it is: disorganized, chaotic, sensitive to initial conditions, 3-D, and consists of a wide range of length and time scales. By expanding upon the current knowledge base through experimental turbulence research, it is possible to improve our understanding of turbulence and apply this knowledge to current industrial interests.

The objective of the work in this thesis is the characterization of a rough surface with flow injection and flow suction boundary conditions applied to a turbulent flow. The rough surface being investigated is similar to that of a thermal protection system (TPS), which is used as a heat-shield to prevent a spacecraft from burning up upon entering an atmosphere. An ablative TPS is designed to ablate, or burn away, when exposed to aerodynamic heating which causes pyrolysis gases to be expelled from

the TPS surface. These gases modify the boundary layer near the surface by reducing the heat flux (also known as "film cooling") through thickening of the thermal layer, blowing a relatively cooler gas into the flow field, and by changing the gas composition near the wall. As the TPS ablates, the carbon phenolic material becomes charred and a characteristic rough surface develops. These roughness features can cause transition to turbulence which greatly increases mass, momentum, and energy transport between the surface and the flow field. These effects must be accounted for in modeling atmospheric entry of spacecraft but cannot be done through direct numerical simulation due to immense cost of computing in resolving the small scale surface features. Thus, the effect of these surface features on the flow field must be modeled. However, for any given surface roughness topology, there is currently no universal model which is able to predict the turbulent behavior. Due to the wide range of roughness geometries and certain discrepancies in properly defining surface roughness, current approaches use heating augmentation factors which have been empirically derived as opposed to predicting TPS performance based upon a known roughness geometry. By properly characterizing a rough surface through its effects on wall shear stress, it is possible to gain a better understanding of how to model that surface roughness which can be applied to future heat shield designs.

In the work described here, the wall shear stress of a fibrous roughness with mass injection through the surface was measured. To do so, a turbulent channel flow apparatus was designed and constructed which could produce fully-developed, one-dimensional flow. These flow conditions were required to allow the wall-shear stress to be determined from the velocity field characteristics as the combination of roughness and blowing boundary conditions made other available approaches to measure wall shear stress either impossible or impractical. It is the goal of this research to provide validation data for turbulence models as well as helping to better understand modification of wall shear stress on a rough surface due to momentum injection.

Chapter 2 Background

2.1 Basic Turbulence Theory

As previously mentioned, turbulence can be thought of as fluid flow that is disorganized, chaotic, and seemingly random. It consists of large scale motions that contain the bulk of turbulent kinetic energy. These large structures then diffuse and dissipate by the action of viscous forces into smaller-scale structures. This process continues until the kinetic energy is converted into thermal energy at the smallest scales of turbulence. Pioneering work on the transition to turbulence was conducted by Osbourne Reynolds [6] who observed the transition to turbulent flow by injecting streaks of dye into a smooth-walled transparent pipe. This lead him to define a dimensionless parameter, now known as the Reynolds number

$$Re = \frac{UL}{\nu} \tag{2.1}$$

where U is the streamwise velocity, L is the characteristic length, and ν is the kinematic viscosity. This ratio expresses the relationship between inertial and viscous forces of a given fluid flow. Expanding upon these ideas in a later paper [7], he developed what is now called Reynolds decomposition whereby

$$\vec{U} = \vec{\overline{U}} + \vec{u}'. \tag{2.2}$$

In Cartesian coordinates, $\vec{U}$ is the velocity vector which contains components U, V, W and depends upon all three spatial coordinates x, y, z and time, t. $\vec{\overline{U}}$ represents the

time-independent mean velocity vector which contains components $\overline{U}, \overline{V}, \overline{W}$ and $\vec{u}'$ represents the fluctuating, time-dependent, components u', v', w'. This decomposition was a fundamental part in the development of various analytical approaches to turbulence and more specifically, the Reynolds Averaged Navier-Stokes (RANS) equations. The Navier-Stokes equation for incompressible, Newtonian flow is given by

$$\vec{U}_t + \vec{U} \cdot \nabla \vec{U} = -\nabla \vec{P} + \nu \Delta \vec{U} + \vec{F}_B \tag{2.3}$$

where the subscript t denotes time differentiation, $\partial/\partial t$. $\vec{P}$ is the pressure vector which has been divided by constant density. $\vec{F}_B$ represents the body forces that have also been divided by constant density. The differential operators ∇ and Δ are the gradient and Laplace operators, respectively. The kinematic viscosity is denoted by ν. Equation 2.2 is then implemented by substituting it into equation 2.3. The resulting equation is then simplified through applying time-averaging, which reduces $\vec{u'}$ to zero. Ultimately, the equation is reduced to the RANS equation

$$\nabla \cdot \vec{\overline{U}}^2 + \nabla \cdot \vec{\overline{u'^2}} = -\nabla \vec{\overline{P}} + \nu \Delta \vec{\overline{U}} \tag{2.4}$$

In this thesis, the RANS equation is used to show how direct measurement of the wall shear stress can be obtained through certain assumptions of the flow geometry.

2.2 Turbulent Wall-Bounded Flow

Another aspect to turbulence which was advanced soon after the work of Reynolds, was that of boundary layer theory. Ludwig Prandtl [8] first described wall-bounded shear flow, as well as other topics such as drag development, flow separation and aircraft stall. In his paper [8], he developed the idea of separating wall-bounded flow into two distinct regions called the inner and outer layers. In the inner layer, which is a region very close to the wall, the flow is dominated by viscous effects. The velocity

profile in this region varies linearly perpendicular to the wall in the turbulent case. In a later work by Prandtl [9] he studied the flow behavior at high Reynolds numbers and determined that the inner layer depends only on kinematic viscosity, ν, and the wall shear stress, τ_ω. Using these parameters, a velocity scale can be defined called the friction velocity

$$U_\tau = \sqrt{\frac{\tau_w}{\rho}} \tag{2.5}$$

where ρ is the fluid density. From this definition, a length scale can also be developed called the viscous length.

$$\delta_\nu = \frac{\nu}{U_\tau} \tag{2.6}$$

In the outer layer the velocity profile from the wall remains nearly constant. In this region, the flow depends less on viscous effects and more on inertial effects. In addition to U_τ, the relevant scales here are the characteristic length, such as the channel half-height h, and area-averaged streamwise velocity U_b (or, alternatively, centerline velocity U_{cl} or the velocity external to the boundary layer, U_e). At intermediate distances there exists an overlap region where both inner and outer scalings are valid. This range can be defined where the distance from the wall, y, satisfies the conditions

$$\frac{yU_\tau}{\nu} >> 1 \quad \text{and} \quad \frac{y}{h} << 1 \tag{2.7}$$

Prandtl also argued that within this region, the inner and outer layers must be related in that the velocity gradient depended upon the ratio of friction velocity and the distance from the wall, multiplied by a function of wall distance normalized by δ_ν [9]. This can be expressed by

$$\frac{dU^+}{dy^+} = \frac{1}{\kappa y^+} \tag{2.8}$$

where the + superscript denotes scaling with the viscous units, U_τ and δ_ν. $\kappa \approx 0.4$ is

the von Kármán constant which was initially believed to be universal. However, its universality is still under debate [14], spurred in part by ambiguity in the definition of the location of the overlap layer (sometimes considered to be $y^+ > 50, \frac{y}{h} < 0.1$ although the exact range is still an active area of research). Theodore von Kármán then took these ideas and developed what is widely known as the logarithmic law on the wall [10] in which equation 2.8 is integrated to form

$$U^+ = \frac{1}{\kappa} \ln y^+ + B \tag{2.9}$$

where B is a constant of integration and represents a shift in the mean flow due to the flow geometry.

2.3 Channel Flows With Smooth Walls

Channel flow, also known as duct flow, has been extensively studied due to its applicability in many industrial operations as well as its simplicity for experimental and computational investigation into near-wall effects. Nikuradse [11] and Reichardt [12] were first credited with investigating fully-developed turbulent channel flow. Nikuradse was interested in the mean flow whereas Reichardt focused on the velocity fluctuations in the streamwise and wall-normal directions (u', v'). A key distinction between duct and channel flow is that the geometry of channel flow is such that the aspect ratio $(\frac{b}{H})$ is large enough that the flow is statistically independent in the spanwise direction, where b is the width of the channel and H is the height of the channel,

Channel flows can be classified alongside pipe flows as "internal" flows. This is in contrast to"external" flows where the boundary layer is free to grow due to no wall restriction. Hence, fully-developed channel flows and pipe flows are statistically independent of the streamwise direction whereas there is weak streamwise dependence

in external boundary layers. The outer length scales for internal flows is the half-height, h, for channel flows and the radius, R, for pipe flows. Since the outer length scale is fixed, δ_ν becomes increasingly small with increasing Reynolds number [13]. A descriptive Reynolds number for wall-bounded flows is the friction Reynolds number that represents the ratio of outer to inner length scales, which for channel flows is

$$Re_\tau = \frac{hU_\tau}{\nu}. \tag{2.10}$$

In order for there to be enough separation between the large and small scale turbulent motions, Re_τ needs to be relatively high. This allows for the formation of the log-law (equation 2.9) in the overlap region between in the inner and outer layers. Note that the Re_τ at which this occurs depends on the range of y selected for definition of the overlap region.

At the wall, the velocity profile must satisfy the no-slip condition ($U, V, W = 0$). This leads to τ_w being dependent only upon the viscous stresses which can be shown by

$$\tau_w = \rho\nu \left[\frac{d\langle U\rangle}{dy}\right]_w. \tag{2.11}$$

where $\langle U\rangle$ is the average streamwise velocity. This can then be normalized using a reference velocity such as the bulk streamwise velocity, U_b. The skin-friction coefficient can then be defined by

$$c_f = \frac{\tau_w}{\frac{1}{2}\rho U_b} \tag{2.12}$$

Dean [14] investigated the Reynolds number dependence of skin-friction as well as other bulk flow parameters such as centerline velocity, U_{cl}, in two-dimensional channel flow. Dean also verified that there was no dependence on the aspect ratio of the channel for $\frac{b}{h} > 7$. Figure 2.1 shows both the laminar and turbulent correlations of experimental data compiled by Dean [14]. He also investigated the Reynolds number dependence of the log-law (equation 2.9) constants κ and B. These constants should

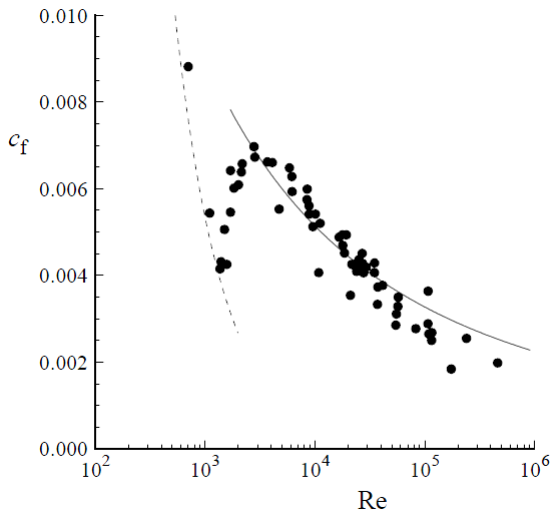

Figure 2.1: Skin-friction coefficient $c_f = \frac{\tau_w}{\frac{1}{2}\rho(U_{cl})^2}$ vs. Reynolds number $Re = 2U_{cl}\frac{\delta}{\nu}$ for channel flow. Dashed line, laminar friction law; solid line, turbulent friction law. Plot taken from Pope [1]

remain invariant, but his results showed a slight increase with increasing Reynolds number. These results were also seen in experiments by Skinner [15] and Hussain and Reynolds [16]. Dean concluded that more experimental investigation was needed, but that the values of $B = 2.12$ and $\kappa = 0.41$ were sufficient to be representative of two-dimensional, high aspect ratio channel flow.

2.4 Rough-Walled Turbulence

To further complicate wall-bounded flows, surface roughness can also have an impact on the turbulence. Rough-walled turbulence is often encountered in real world flows such as around turbine blades, automobiles, aircraft wings, and over the surface of the earth. This roughness affects the near-wall viscous region and promotes an increase in skin-friction, and subsequently, drag and heat transfer. In its simplest form, roughness elements are often described by their individual height, k. While this is sufficient for uniform roughness geometries, there is a need for a more specialized classification when the geometry becomes more complex. This section will outline

some of the different methods in quantifying surface roughness as well as outlining how it modifies the mean flow.

One of the most notable early investigations into surface roughness is by the work of Nikuradse [17]. He experimented with various types of uniform surface roughness in which he sifted sand grains of a known size to produce a roughness pattern on the inside of pipes. He measured the friction factor, f which is defined by

$$f = \frac{\Delta p D}{\frac{1}{2}\rho U_b^2 L} \tag{2.13}$$

where D is the pipe diameter, and Δp is the pressure drop over the axial distance r in pipe flow. Nikuradse varied the ratio of pipe radius to roughness height of the sand grains, R/k and looked at the dependency with increasing Reynolds number which is seen in figure 2.2. It can be seen that at low Reynolds number, the flow

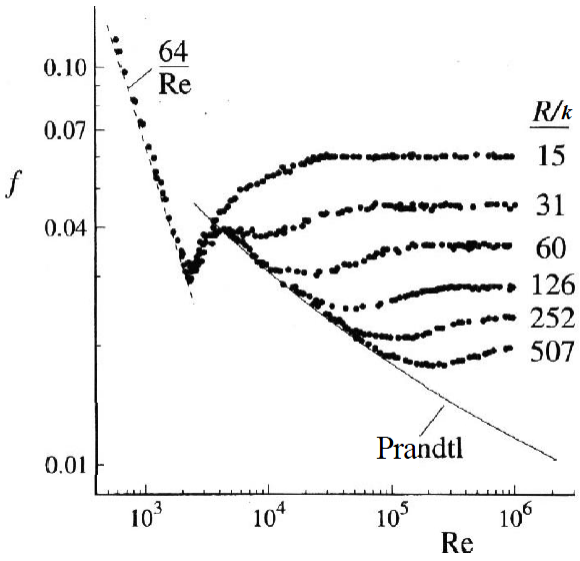

Figure 2.2: Nikuradse's measurements of friction factor f vs Reynolds number for various sand grain sizes in pipe flow. Plot taken from Pope [1], adapted from [2]

is unaffected by the roughness in the laminar regime and the behavior is similar to smooth-walled flow. There is also little effect as the flow transitions to turbulence. At higher Reynolds number, each of the different grain size cases follow Prandtl's

smooth wall correlation until each of the trends asymptotes and loses dependence on Reynolds number. It is at this point that the flow in the presence of wall roughness is considered to be fully-rough. Figure 2.2 is used as an example to characterize the rough surface utilized in this thesis and will be discussed later.

The observed behavior in fig. 2.2 can be explained through a modification to eq. 2.9 to account for roughness effects. There are extensive review papers by Raupach [18] and Jiménez [19] in which they describe these effects in detail. It is known that roughness affects the mean flow by displacing it upwards away from the wall by some amount y_o, called the zero-plane displacement which depends upon both the flow and roughness geometry. While the exact definition of this value is still up for debate, as there are multiple methods for determining y_o as described in [18], it follows that $0 < y_o < k$. This can then be used to define the displaced distance away from the wall given by

$$Y = y - y_o. \tag{2.14}$$

As follows in [18] there is an asymptotic matching analysis for $U(Y)$ to account for mean flow effects due to roughness. In the outer layer, where $U(Y)$ depends on the outer length scale h for channel flow, the velocity dependency can be defined by the defect law given by

$$\frac{U(Y) - U_{cl}}{U_\tau} = G(Y/h) \tag{2.15}$$

where R is utilized as the length scale for pipes, and external velocity U_e and boundary layer thickness δ are utilized as the velocity and length scale for boundary layers. In the inner layer, where $U(Y)$ depends on viscous scaled terms, another velocity dependency can be defined given by

$$\frac{U(Y)}{U_\tau} = F(Y^+, k^+, h_i^+) \tag{2.16}$$

where h_i a set of length scales used to fully characterize more complex roughness

geometries. In the overlap region of wall-bounded flow ($y^+ > 50$), the inner and outer velocity laws must be valid, the leads to a gradient matching given by

$$\frac{Y}{U_\tau}\frac{dU}{dY} = Y^+\frac{dF}{dY^+} = \frac{Y}{h}\frac{dG}{d(Y/h)} = \kappa^{-1} \tag{2.17}$$

by integrating 2.17 it is possible to recover a form of equation 2.9 which is modified to account for rough-walled flow given by

$$U^+ = \kappa^{-1}\ln Y^+ + C(k^+, h_i^+) \tag{2.18}$$

where the integration term, C is a function of the roughness length scales. For smooth walls, this term would become a constant value. Equation 2.18 can be re-written to a more commonly used form given by

$$U^+ = \kappa^{-1}\ln Y^+ B + W(Y/h) - \Delta U^+(k^+, h_i^+) \tag{2.19}$$

where the first three terms represent standard smooth wall flow. $W(Y/h)$ is called the wake function and represents the modification of the mean flow due to outer layer effects and describes the difference between the velocity profile and the logarithmic law. The ΔU^+ term is called the roughness function and represents the modification of the mean flow due to roughness and is zero for a smooth wall. It can be understood as the difference between the smooth and rough wall inner-scaled mean velocity profiles.

One of the fundamental ideas that also came from Nikuradse's initial work was that of the roughness height parameter, k_s known as the equivalent sand-grain roughness. This height forms a baseline of comparison to other types of roughness geometries. While there is still some argument over the validity of this parameter to describe

more complex roughness, according to Schlichting [20], it can defined by

$$k_s = 32.6 \frac{\nu}{U_\tau} e^{-\kappa(B-\Delta U^+)} \tag{2.20}$$

which leads to the definition of a Reynolds number to characterize the effects of sand-grain roughness given by

$$k_s^+ = \frac{k_s U_\tau}{\nu} \tag{2.21}$$

It is worth noting that the determination of k_s^+ requires that ΔU^+ is known, which depends on the Reynolds number based on k. Knowing the sand-grain roughness Reynolds number allows a given rough-walled flow to be classified into one of three flow regimes based on the value of k_s^+:

1. $k_s^+ < 5$ The flow is considered to by dynamically smooth with no observable effects of roughness seen in the flow statistics.

2. $5 < k_s^+ < 50$ The flow is transitionally rough.

3. $k_s^+ > 50$ The flow is fully rough where a considerable shift can be seen in ΔU^+.

Another main idea dealing with roughness effects on the mean flow is the wall-similarity hypothesis of Townsend [21]. This states that outside of the roughness sublayer, the turbulent motions are independent of the surface roughness at the wall and also that the interaction between the inner and outer layers are weak at a sufficiently high Reynolds number [22]. In other words, the roughness only acts to change the surface stress leaving the turbulence statistics unaffected. This assumes that the roughness features are significantly smaller than the outer length scale, i.e. $k/h << 1$ for channel flows. While Townsend's hypothesis is generally accepted, there were recent investigations that produced results which contradicted it. Krogstad and Antonia [23] found that the Reynolds stress profiles in the outer layer increased with the addition of surface roughness. Direct numerical simulation (DNS) results from Lee

and Sung [24] also showed significant modification to the turbulence statistics in the outer layer.

A major source of discrepancy for the validity of Townsend's hypothesis is the type of roughness geometry that is under investigation. While k can be used as a simple characterization to roughness, other length scales are required when the geometry becomes two-dimensional or three-dimensional. Volino et al [25] discussed in detail the turbulence structure in boundary layers over periodic 2-D and 3-D roughness. In this case, 2-D spanwise square bars were found to affect the outer layer which is was seen as an increase in the Reynolds stresses, particularly in the wall-normal profile of $-\overline{u'v'}$. This was explained by the growth of flow structures that were much larger than k caused by the width of the square bars which grew into the outer layer and affected the turbulent stresses. This effect was not seen in the 3-D case in which the roughness geometry consisted of transverse rows of staggered cubes. These results suggest that wall-similarity is influenced by dimensional differences between 2-D and 3-D roughness [22].

There is also literature that classifies surface roughness into either d-type or k-type. As laid out in [19], the distinction between d-type and k-type roughness was first made by Perry et al. [26]. For k-type roughness, k_s should be proportional to the roughness dimensions themselves. To be more specific, ΔU^+ at high Reynolds numbers is determined by k. This not the case for d-type roughness where ΔU^+ is independent of k. Instead, turbulence in d-type roughness is dependent upon the thickness of the wall layer, i.e. h, R, or δ. Raupach [18] goes on to further explain some of the difficulties with dividing roughness into these two classes. Namely, that the division implies that ΔU^+ is determined by a single length scale. It has already been discussed how more complex roughness geometry requires a multitude of length scales for its description. Another issue with this division is that d-type roughness invalidates the asymptotic matching analysis which leads to equation 2.9 as explained

in [26]. For δ to truly be an inner layer length scale, a new derivation of the log law must be found.

2.5 Turbulence with Flow Injection

To further expand upon the experimental modeling of an ablative TPS, it is necessary to investigate the turbulent effects due to flow injection, or blowing, through the surface of wall-bounded flow. As with the turbulence effects due to surface roughness, there have been numerous studies into the turbulence effects due to blowing because of its applications in film cooling for turbine blades as well as through laminar flow control on the wings of aircraft to reduce drag. Initial investigations into blowing effects were focused on zero pressure gradient boundary layers over a porous flat plate. It was shown that the addition of blowing reduced skin friction by decreasing the shear stress at the surface [27–30]. Park and Choi [31] described this effect as the streamwise vortices above the wall being lifted up due to blowing which caused the shear interactions between the wall and the vortices to lessen.

The turbulent boundary layer under the influence of blowing can be represented as a modification of the log law (eq. 2.9). Kornilov [32] presents a model for this modification in which the mean flow is given by

$$U^+ = \frac{1}{\kappa} ln(y^+) + B + KU^+_{inj} \tag{2.22}$$

where U^+_{inj} is the inner-scaled injection velocity and K is a constant with weak functional dependence on U^+_{inj} which has the recommended value of 9.6. This added term is analogous to the roughness function, ΔU^+, in that it acts as a modifier to shift the mean flow. In this case, blowing acts on the mean flow by adding momentum and causing a positive shift whereas ΔU^+ acts by removing momentum and causing a negative shift.

There is also evidence that the method of flow injection has a significant effect on the mean flow statistics. Haddad et al [33] conducted an experiment in which a single porous strip was placed upstream in fully-developed channel flow. It was shown that localized blowing did cause modification to the Reynolds stresses, but the effect decreased with increasing distance downstream from the strip. DNS results in which a uniform blowing through a spanwise slot was simulated showed that the streamwise turbulence intensity recovered quickly while the other components of turbulence intensity and Reynolds stresses took longer to recover downstream of the flow [31].

A large study on the transpiration effects on a smooth wall turbulent boundary layer was conducted by Moffat [34] and Kays [35]. This produced a number of observations in which it was seen that for low blowing ratios, there is a near wall region where Couette flow assumptions are valid. It was also seen that in the near wall region ($y/\delta < 0.1$) the mixing-length, which is defined as the distance over which a hypothesized turbulent eddy retains its identity [1], is related by

$$l = \kappa y \tag{2.23}$$

as is the case with flows without transpiration. Moffat also observed that as the transpiration rate increased, that the streamwise velocity profiles become more "rough-like" until they resemble the unblown rough wall profile [34]. These effects were seen in the shrinking of what is called the "knee" in the profile curve. This knee occurs in the buffer zone of the velocity profile at the boundary of the viscous sublayer. With increased flow injection, this knee flattens out and occurs at smaller y/δ. It was concluded that the sublayer thickness decreases with increasing blowing rate. These effects were also alluded to in a work by Reynolds [37]. He mentions that for a high enough blowing rate, that the distribution of pores used for flow injection on an given surface will have some effect on the boundary layer. The pores will result in an array

of jets which, depending on the flow conditions, will have the effect of acting as a solid perturbance to the mean flow. This results in the smooth wall behaving as though it were roughened.

2.6 Turbulence with Surface Roughness and Flow Injection

As previously mentioned, the combination of roughness and blowing effects on turbulent wall-bounded flow presents a field of study which has seen little attention in terms of the quantity of research. This is especially true when compared to studies that focus on roughness and blowing as separate effects. A few studies have been conducted on the combined effects which only focused on the mean flow properties [5, 28, 38, 39]. It was only the work by Schetz and Nerney [39], and more recently Miller [3] that also included analysis on turbulence statistics.

Due to the limited data available as well as the wide range of experimental configurations with regards to flow conditions and geometry, there is little consensus on what the combined effects of roughness and blowing are. It is known that roughness acts to shift the mean profile which is seen in ΔU^+. Voisinet [5] found that the introduction of blowing caused an additional shift in ΔU^+. This result however, was not seen in the work of Schetz and Nerney. Their work did show that blowing increased the turbulence intensity near the wall which is in agreement with the observations discussed in the previous section with blowing over a smooth porous surface.

There is also some confusion with regards to the roughness effects and more specifically, the types of roughness geometries used in each investigation. Roughness geometry is inherently difficult to properly characterize and as a result, a variety of different geometries have been investigated. The work of Healzer [28] dealt with arrays of copper balls which used the ball diameter to represent the roughness height. Voisinet's work [5] used a series of wire meshes which are geometrically very different than that of spherical arrays. Recent work by Miller [3] used a two-dimensional sinu-

soidally varying roughness pattern. In this work it was found that the combination of roughness and blowing caused an increase in skin friction and τ_w which differs from other findings. Ignoring the type of geometry used in each investigation, the overall trend is that roughness acts to remove momentum from the flow whereas blowing acts to add momentum. These effects are represented by the ΔU^+ and KU_{inj} terms in equation 2.22.

The limited knowledge available in this area means there is an interest in collecting empirical data to aid in understanding of roughness and blowing effects. This interest is fueled in part, by the applications in the aerospace industry with regards to TPS technology. Computational Fluid Dynamics (CFD) modelers can also make use of this data to validate their code and refine turbulence models. This thesis can expand upon the knowledge base by producing valid data on the combination of these effects.

2.7 Measurement of Wall Shear Stress

A key objective of the work in this thesis is focused on the measurement of τ_w. Furthermore, this measurement allows determination of c_f which is used to scale results for use in engineering systems. By plotting this value across a range of Reynolds numbers it is possible to predict the drag effects on the flow induced by the surface geometry under investigation. However, the combination of roughness and blowing effects makes the measurement of this quantity experimentally very challenging. An in depth discussion of wall shear stress measurement techniques can be found in [40]. This section gives a brief overview of the basic techniques and also the difficulties encountered with measuring τ_w for flows having roughness and blowing.

Many of the methods involve obtaining measurements directly on the surface. One such method is called oil-film interferometry (OFI). This technique makes use of the fringe pattern that is produced when light is reflected off a thin layer of oil on the surface of wall-bounded flow. First utilized by Tanner and Blows [41], OFI requires the

measurement of the oil film thickness which is directly related to the shear stress that the flow imparts to the oil. The difference in film thickness, Δs between successive fringes is given by

$$\Delta s = \frac{\lambda}{2(n^2 - \sin^2 \alpha)^{1/2}} \tag{2.24}$$

where λ is the wavelength of light, α is the observer viewing angle, and n is the refractive index of the oil. Collecting this measurement over a time period allows for calculation of the thinning rate. For a sufficiently thin film under two-dimensional flow, the thinning rate is related to τ_w by

$$\frac{\partial s}{\partial t} = -\frac{1}{2\mu} \frac{\partial(\tau_w h^2)}{\partial x}. \tag{2.25}$$

This method requires a smooth surface to allow the relationship between fringe patterns and wall shear stress.

Another surface technique for measuring τ_w in internal geometries is through the measurement of the mean pressure gradient. Through a control volume analysis on fully-developed pipe or channel flow with a constant cross sectional area A_c, the average τ_w can be determined by a relationship between the pressure drop over a length of duct which is given by

$$\Delta P A_c = \int_A \tau_w dA \tag{2.26}$$

which for fully-developed flow, τ_w per unit length of channel is constant. This leads to

$$\tau_w = \frac{\Delta P}{2L} h \tag{2.27}$$

In order to obtain fully-developed flow conditions for blowing cases, the mass flux through the channel must remain constant and hence there must be suction on the opposite surface. However, the pressure gradient is related to the average of the

wall shear stress over all surfaces and if there is both suction and blowing, it is not possible to separate the contribution of blowing and suction surfaces from the shear stress determined from the pressure gradient.

A method that also involves a pressure difference measurement is through the use of Preston tubes. These tubes were first developed and utilized by Preston [42] and are essentially Pitot tubes that are placed near but not directly on the wall. The tubes are situated within the logarithmic region of the law-of-the-wall and capture the stagnation pressure produced by the mean velocity. Through dimensional analysis of the region, an expression can be found correlating τ_w and ΔP given by

$$\frac{\Delta P}{\tau_w} = f(\frac{d^2\tau_w}{\rho\nu^2}) \tag{2.28}$$

where ΔP is the mean pressure difference between the Preston tube and the static pressure from a nearby wall tap, and d is the outer diameter of the Preston tube. This technique requires calibration against a well defined flow field such as fully-developed pipe flow in which τ_w can be independently determined. Channel flow geometry with the combination of roughness, blowing, and suction effects have not shown that the law-of-the-wall exists which is a prerequisite for the use of Preston tubes.

Another technique that requires the existence of the log-law is the Clauser method. Clauser [43] first observed that τ_w could be estimated in turbulent boundary layers through correlation with the law-of-the-wall. In order to use this correlation, equilibrium flow conditions must be met in which the statistical profiles can be represented in a self-preserving form using locally determined integral parameters [40]. The Clauser method is a graphical method in which τ_w is found by matching the inner-scaled streamwise velocity profile to the log-law (eq. 2.9). A benefit to this approach is that flow information in the viscous sublayer near the wall which is often difficult to obtain is not needed. As previously stated however, the flow conditions and geometry used

in this work have not shown that the logarithmic law exits which limits the use of this method. It should be noted that Miller [3] did use this approach, but found that their trends in τ_w with increasing blowing were counter to those previously observed.

Wall-mounted sensors such as hot-wire and hot-film probes have also been commonly used to measure τ_w. These instruments have the ability to be mounted directly near the wall under investigation. The problem for utilizing them in this work is that they require a calibration against a known shear stress and precise knowledge of their distance from the wall. While this would have been feasible, there would have needed to have been greater modification to the wind tunnel used in this experiment that could support a mount for such instrumentation inside of the test section. These instruments are typically reserved for smooth-wall measurements due to the difficulty in measuring near the surface of rough geometry.

One of the simplest methods to acquiring τ_w is by direct measurement through the use of floating element sensors such as drag plates and force balances. These devices are placed on the wall and work by measuring the shear force that is imparted on the floating element portion when exposed to the flow. This is accomplished by either measuring the amount of force needed to keep the floating element in place or by measuring the displacement and correlating it with the applied shear force. A major advantage to using these devices is that the direct shear measurement does not require any assumptions about the flow field or fluid properties in order to be valid [40]. They also do not require a correlating function (i.e. calibration) with a known flow field. This removes some of the errors associated with calibration which can be seen in the use of other direct methods such as with hot-film probes. These sensors are not without disadvantages, some of which are outlined by Winter [44]. For one, there is a balance that needs to be maintained where the floating element is large enough that a force of sufficient magnitude can be measured while also being small enough that the element can measure the local flow conditions. Problems can

also arise with the edges around the sensor introducing adverse effects into the flow that are uncharacteristic of the flow under investigation. These issues along with the technical challenges involved in maintaining uniform blowing and roughness through the surface balance resulted in the decision to find an alternative approach to measure τ_w.

2.8 Measurement of Wall Shear Stress through the use of the RANS Equation

Given the lack of suitable direct techniques to measure τ_w for flows with combined roughness and blowing, an alternative approach was required. The work in this thesis uses certain assumptions about the flow geometry along with the Reynolds Averaged Navier-Stokes (RANS) equations to relate τ_w to measurable flow quantities.

To begin the derivation, a diagram of the channel flow geometry is shown in fig. 2.3. The basic configuration consists of a standard channel flow setup in which the

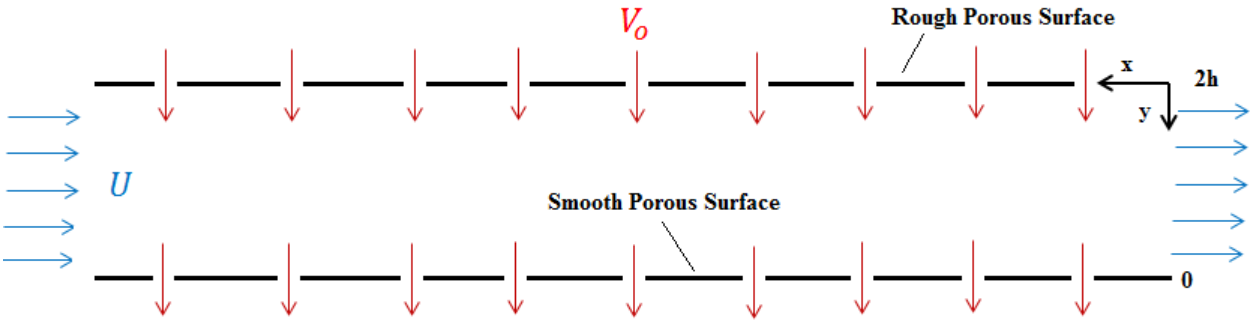

Figure 2.3: Diagram of the channel at the test section with a rough top surface along with blowing and suction boundary conditions for the top and bottom walls.

aspect ratio (b/h) is large enough such that the flow is statistically independent in the spanwise, z-direction. This allows a crucial assumption to be made in which the spanwise terms can be ignored making the flow two dimensional. Beginning with the

mean continuity equation, where the angle brackets indicate an ensemble average,

$$\frac{d\langle U\rangle}{dx} + \frac{d\langle V\rangle}{dy} + \frac{d\langle W\rangle}{dz} = 0 \tag{2.29}$$

and applying the 2-D assumption, eq. 2.29 can be reduced to

$$\frac{d\langle U\rangle}{dx} + \frac{d\langle V\rangle}{dy} = 0 \tag{2.30}$$

it is also possible to apply the assumption that the flow is fully developed, which removes streamwise dependence. This simplifies eq. 2.30 to

$$\frac{d\langle V\rangle}{dy} = 0 \tag{2.31}$$

integrating eq. 2.31 yields

$$\langle V\rangle = V_0 \tag{2.32}$$

where V_0 is the flow injection/suction velocity, which remains constant.

Moving on, the incompressible RANS equation for 2-D flow is given by

$$\rho\left(\frac{\partial\langle U_i\rangle}{\partial t} + \frac{\partial\langle U_iU_j\rangle}{\partial x_j} + \frac{\partial\langle u_i'u_j'\rangle}{\partial x_j}\right) = -\frac{\partial\langle p\rangle}{\partial x_i} + \mu\frac{\partial^2\langle U_i\rangle}{\partial {x_j}^2} \tag{2.33}$$

where $i = 1, 2$ and $j = 1, 2$ which correspond to the streamwise and wall-normal components x, y respectively. Assuming steady flow, the first time-varying term can be removed giving

$$\rho\left(\frac{\partial\langle U_iU_j\rangle}{\partial x_j} + \frac{\partial\langle u_i'u_j'\rangle}{\partial x_j}\right) = -\frac{\partial\langle p\rangle}{\partial x_i} + \mu\frac{\partial^2\langle U_i\rangle}{\partial {x_j}^2} \tag{2.34}$$

Looking at the case where $i = 1$

$$U\frac{\partial\langle U\rangle}{\partial x} + V_0\frac{\langle U\rangle}{\partial y} + \frac{\partial\langle u'^2\rangle}{\partial x} + \frac{\partial\langle u'v'\rangle}{\partial y} = -\frac{1}{\rho}\frac{\partial\langle p\rangle}{\partial x} + \nu\left[\frac{\partial^2\langle U\rangle}{\partial x^2} + \frac{\partial^2\langle U\rangle}{\partial y^2}\right] \tag{2.35}$$

which can be simplified further by applying the fully-developed assumption to the x-dependent velocity terms, this yields

$$V_0\frac{\langle U\rangle}{\partial y} + \frac{\partial\langle u'v'\rangle}{\partial y} = -\frac{1}{\rho}\frac{\partial\langle p\rangle}{\partial x} + \nu\frac{\partial^2\langle U\rangle}{\partial y^2} \tag{2.36}$$

Looking at the case where $i = 2$

$$U\frac{\partial\langle V_0\rangle}{\partial x} + V_0\frac{\langle V_0\rangle}{\partial y} + \frac{\partial\langle v'^2\rangle}{\partial y} + \frac{\partial\langle v'u'\rangle}{\partial x} = -\frac{1}{\rho}\frac{\partial\langle p\rangle}{\partial y} + \nu\left[\frac{\partial^2\langle V_0\rangle}{\partial x^2} + \frac{\partial^2\langle V_0\rangle}{\partial y^2}\right] \tag{2.37}$$

which can also be simplified by applying the fully-developed assumption to the x-dependent velocity terms as well as removing the V_0 terms which do not vary spatially giving

$$\frac{\partial\langle v'^2\rangle}{\partial y} = -\frac{1}{\rho}\frac{\partial\langle p\rangle}{\partial y}. \tag{2.38}$$

The boundary condition $\langle v'^2\rangle = 0$ at the rough wall is then applied to eq. 2.38 and integrated to produce

$$\langle v'^2\rangle + \frac{\langle p\rangle}{\rho} = \frac{p_w}{\rho} \tag{2.39}$$

where $p_w = \langle p(x, 0, 0)\rangle$ is the pressure at the rough wall. Since the pressure gradient is uniform across the across the top and bottom walls of the channel, it can be said that

$$\frac{\partial\langle p\rangle}{\partial x} = \frac{\partial p_w}{\partial x}. \tag{2.40}$$

Eq. 2.36 can be rearranged and solved for $\partial\langle p\rangle/\partial x$ giving

$$\frac{\partial\langle p\rangle}{\partial x} = \frac{\partial p_w}{\partial x} = \rho\nu\frac{\partial^2\langle U\rangle}{\partial y^2} - \rho\frac{\partial\langle u'v'\rangle}{\partial y} - \rho V_0\frac{\langle U\rangle}{\partial y} \tag{2.41}$$

Now let the shear stress at any point in the flow be given by

$$\tau = \rho\nu\frac{\partial\langle U\rangle}{\partial y} - \rho\langle u'v'\rangle - \rho V_0\langle U\rangle \tag{2.42}$$

From equation 2.41 we get

$$\frac{\partial\tau}{\partial y} = \frac{\partial p_w}{\partial x}. \tag{2.43}$$

Integrating eq. 2.43 with respect to y produces an equation which allows the determination of the vertical shear stress profile given by

$$\tau(y) = \frac{\partial p_w}{\partial x}y + \tau_w. \tag{2.44}$$

It is worth noting that for the standard smooth wall channel flow geometry, the shear stress profile is asymmetric about the half-height, h. This allows the application of the boundary condition to eq. 2.44 that $\tau(h) = 0$. This yields

$$0 = \frac{\partial p_w}{\partial x}h + \tau_w \tag{2.45}$$

which upon simplifying gives

$$\frac{\partial p_w}{\partial x} = -\frac{\tau_w}{h}. \tag{2.46}$$

Substituting eq. 2.46 into eq. 2.44 gives

$$\tau(y) = \tau_w\left(1 - \frac{y}{h}\right) \tag{2.47}$$

which is valid for the smooth-walled case. For the rough-walled case with blowing and suction, it cannot be assumed that the shear stress will be zero at the half-height. The value of τ_w on the top rough wall will be different from that on the bottom smooth wall. This will cause a shift in the zero crossing in the profile away from h. In this case, it can be assumed that at some point in the profile, the shear stress will

be zero. This can be defined as $\tau(y_{\tau_0}) = 0$ which leads to a new expression for the vertical shear stress profile given by

$$\tau(y) = \tau_w \left(1 - \frac{y}{y_{\tau_0}}\right). \tag{2.48}$$

This equation is linear and does not require a pressure gradient measurement. In order to determine τ_w on the rough wall, all that is needed is to measure each of the terms given in eq. 2.42 at enough points to produce a vertical profile which can be linearly extrapolated to the rough wall. However, in order to do so one must have fully-developed channel flow. The next chapter will outline the experimental setup developed to achieve these conditions.

Chapter 3 Experiment Design

The previous chapter discussed a method that would allow the measurement of τ_w on a surface within a channel which required knowledge of certain parameters in the flow itself. This meant that an experiment had to be developed to allow those parameters to be known. The experiment consisted of a turbulent channel flow facility to generate the desired flow, and a particle image velocimetry (PIV) system to measure the flow statistics. The TCFF had to meet certain criteria to match the assumptions (namely, fully developed flow, uniform blowing, a certain range of blowing rates and Reynolds numbers, etc.). Details of the facility and measurement system are provided in sections 3.1 to 3.6

3.1 Facility Description

The experiments for this thesis were conducted in the turbulent channel flow wind tunnel located in the Experimental Fluid Dynamics Lab (EFDL) at the University of Kentucky. The development of this facility is described in detail in Estejab [45] and was designed to produce turbulent plane Poiseuille flow as well as be large enough to maximize the Reynolds number given the available lab space. To accomplish this, the channel flow wind tunnel was built with a channel half height of $h = 50.8$ mm and an aspect ratio of 9:1 to ensure that the 2-D flow conditions were met [46]. It was also necessary to ensure that there were no streamwise velocity and Reynolds stress gradients in the flow at the test section. This was accomplished by building the channel long enough to produce fully developed turbulent flow. This

length was determined to be $246h$ from the channel inlet to the test section [47]. In addition to the $24h$ test section, there is a $12h$ section at the exit which ensures that the pressure gradient remains constant throughout the measurement section. The turbulent channel flow facility is powered by a 5.2 kW centrifugal blower used to drive the flow through conditioning, contraction, and development sections. This blower allows for bulk flow velocities, U_b, up to 30 m/s and consequently, Reynolds numbers up to 102,000. A strip of 50 mm wide, 120 grit sand paper followed by another 100 mm wide, 60 grit strip was placed at the development section inlet to act as a fixed turbulent transition point. A schematic of the wind tunnel with the smooth wall configuration can be seen in fig. 3.1.

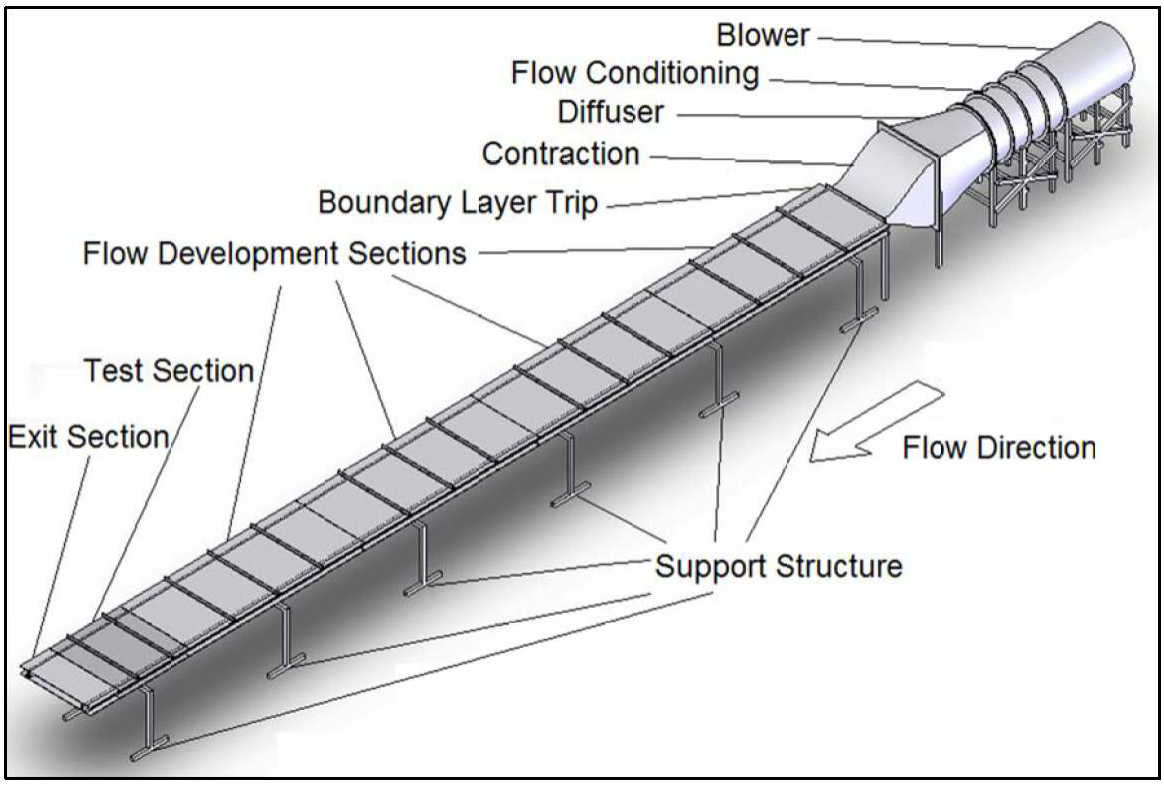

Figure 3.1: Schematic of the turbulent channel flow facility with the smooth-wall configuration before current modifications.

The smooth-walled channel configuration was then modified to support the work of Miller [3]. He investigated the roughness and flow injection effects on the turbulent

boundary layer through analysis of the turbulence statistics on an idealized, quasi-two dimensional rough surface. The changes that were made was the addition of a flow injection rig which was capable of producing blowing ratios given by the equation

$$BR = \frac{V_0}{U_m} \tag{3.1}$$

of up to 0.729 % [3] for low Reynolds number cases where V_0 represents the injection velocity normal to the rough surface and U_m represents the maximum measured velocity in the channel. This blowing rig was designed to simulate the ablation process by producing a backplane pressure on the 2-D sinusoidal rough surface. The pressure then forces the flow through the micro-cracked pores that are uniformly distributed on the surface. To effectively vary the injection velocity, a reliable method of flow control and velocity measurement was needed. In Miller's blowing rig, the injected flow was supplied by a centrifugal blower (McMater-Carr part number 1963K15). This blower is capable of producing flow rates up to 200 CFM at a static pressure of 350 Pa and was over-sized to allow for the large range of BR previously mentioned. From the blower exit, a reducing section was attached which reduced the square down to a three inch diameter tube. The tube was connected to a 1 meter flexible hose of the same diameter which helped to prevent the blower vibrations from reaching the blowing rig. This was then connected to a section of Schedule 40 black steel threaded three inch diameter pipe. To measure the flow rate, a venturi meter was connected to the steel pipe. After the venturi meter, the flow traveled through an elbow which directed the air into a fixed pattern diffuser (McMaster-Carr part number 1837K21) connected at the top of the blowing rig.

The actual blowing rig consisted of three main sections. Each section was separated by flow conditioning screens used to help remove any adverse flow effects and allowed for uniform flow injection at the rough surface. The entire blowing rig was constructed

from 1 mm thick 3003 Aluminum sheet metal which was desirable due to it's light weight and ease of machining. A schematic of Miller's blowing rig can be seen in fig. 3.2. The geometry of the rig was such that inner dimensions were 0.4572 m in height, 0.889 m in width, and 1.143 m long. The upper section was 152.4 mm in height and was originally designed to house the fans which supplied the injected flow. Certain difficulties were encountered which required the redesign of the upper section to be completely enclosed with the injected flow supplied by an external blower. In between the upper and middle sections was a flow conditioning screen with a mesh size of 3.4 mm (McMaster-Carr part number 9275T38). The middle section was 203.2 mm after which was placed a finer flow conditioning screen with a mesh size of 1.25 mm (McMaster-Carr part number 87655K132) between it and the lower section. It was determined that the middle section be large enough that the spacing between the mesh screens be at least sixty times the mesh size [48]. The final lower section was built with a height of 101.6 mm. An aluminum honeycomb (Bellcomb Industries part number BSP245C) was placed in the middle section on top of the 1.25 mm mesh screen for additional flow conditioning. The rough surface used in Miller's work was mounted to a 3.81 cm lip around the edge of the box. This lip was also used to situate the blowing rig on top of the channel. While these modifications were sufficient for Miller's work, several problems were encountered which required additional modifications to be made. The next section will discuss these changes and their implications on the work in this thesis.

3.2 Current Modifications

Several conclusions were made from [3] regarding the blowing design based on the results gathered. As mentioned in the previous chapter, it was found that the effects of flow injection acted to increase rather than decrease τ_w which was counter to previous investigations. It was hypothesized that the flow may not have been fully-

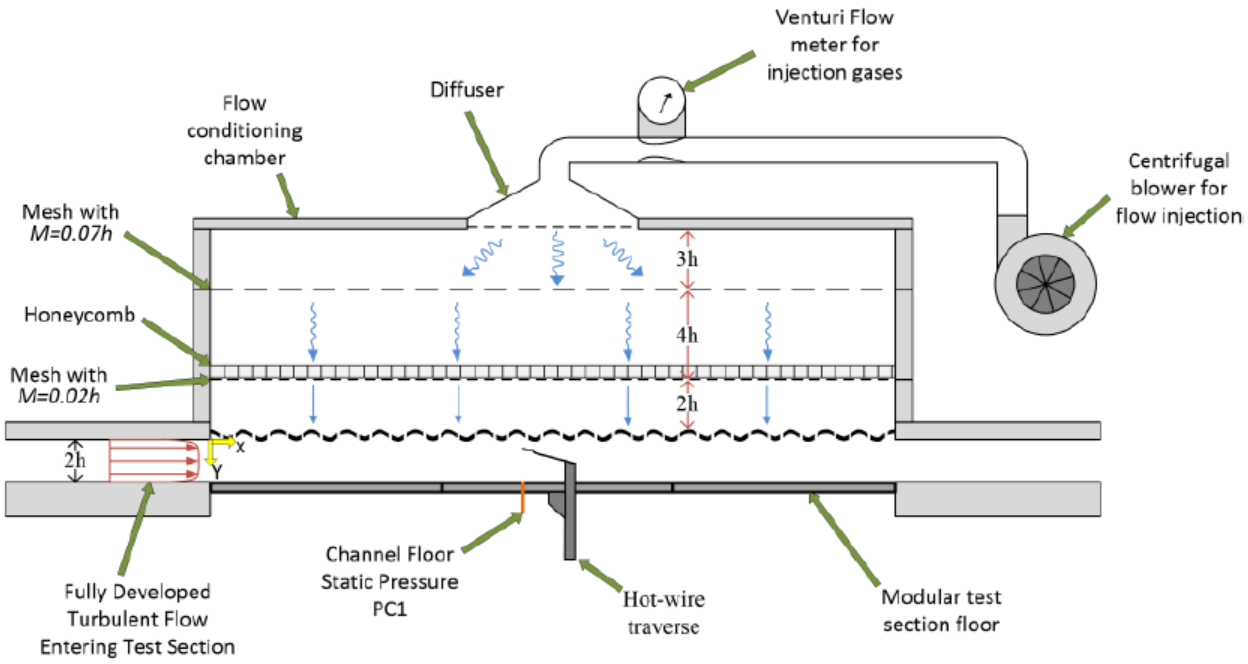

Figure 3.2: Schematic of Miller's blowing rig as described in [3].

developed or that the small BR that were tested may not have been large enough to have a significant adverse effect on the flow. These hypotheses, among other design considerations, motivated the current blowing rig to be designed with the following modifications:

1. Modify the channel to allow for fully-developed flow and preventing injected mass flux from increasing the net mass flux through the channel.

2. Increase the maximum allowable BR to at least 1% to correspond with expected species emission rates experienced by an ablative TPS.

3. Allow optical access at the test section to allow the use of a PIV system to measure flow velocities.

In order create fully-developed flow, the rough surface needed to be extended further upstream in the channel to allow the roughness effects to permeate throughout the channel half-height. This required an additional $60h$ of rough surface with flow in-

jection on top of the $24h$ length in Miller's blowing rig. To accomplish this, a larger blowing rig frame had to be constructed. This frame was largely similar to Miller's rig but designed to allow for an extended rough flow development section. It was also constructed out of 1 mm thick 3003 Aluminum sheet metal that was then cut into strips that were then bent into C-shaped channels. The current blowing rig features the same three sections as described in section 3.1 with the same dimensions of height. The lengths of each of the sections had to be increased to accommodate the larger rough surface area. Due to the larger length, the streamwise side sections had to be split up into two pieces which were then fastened together by an external aluminum brace that was pop-riveted to each piece. The streamwise and spanwise pieces of each section were pop-riveted together to form a complete rectangular frame with inner dimensions of 4.191 m by 0.914 m. The frames of each section once completed, were relatively flimsy due to the thin sheet metal that was used. It was determined that a series of spanwise support structures would be used keep the frames rigid. These supports were formed out of the same aluminum stock and were placed at 1.047 m intervals along the length of the frame. The supports were also pop-riveted to the inside of the frame. Once each of the sections were mounted together, the supports aligned and formed a divider between each of the four blowing sections in the rig. The lower supports were modified further to act as a mounting piece for the rough surface. Each support was cut in half and a 38.1 mm slot was milled into the lower halves. This slot functioned as a fine adjustment for the rough surface in order to properly align it with the inside of the channel. The actual rough surface, which will be discussed more in detail in section 3.4, was mounted to a 6.35 mm thick perforated PVC sheet (McMaster-Carr part number 92985T59). This PVC sheet provided support for the rough surface and featured and array of 12.7 mm diameter holes which allowed the injected flow to reach the inside of the channel. An exploded technical drawing of the blowing rig frame is shown in fig. 3.3.

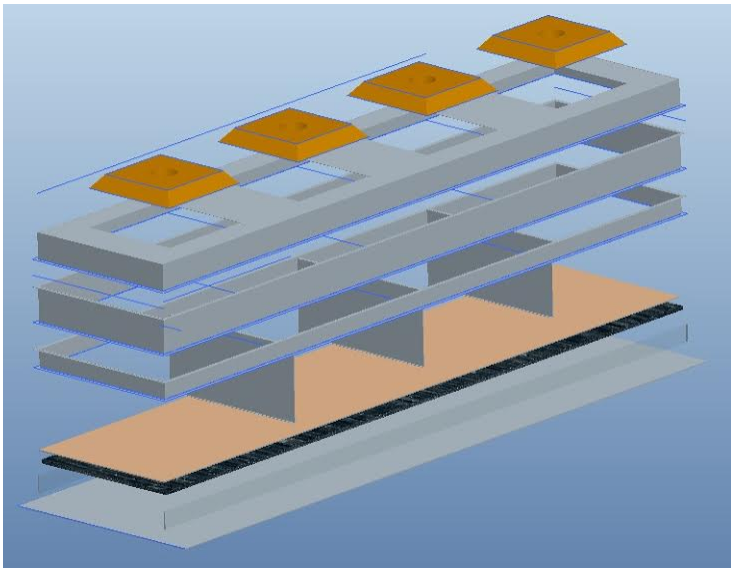

Figure 3.3: Schematic of the current blowing rig frame.

The next issue that needed to be addressed was developing a way to increase the maximum BR to at least 1%. This was a sizing problem to ensure that the blower used would produce the needed mass flow rate. The first step was to measure the system resistance constant, K, for Miller's original blowing rig with the new rough surface added in. This was accomplished by using a handheld anemometer which was placed inside of the channel near the rough surface to capture the injected flow. Using the inner area of the blowing rig of 1.0 m^2 and multiplying by the average velocity of the injected flow at the surface it was possible to determine the volumetric flow rate, Q. For Miller's configuration using the new rough surface, a Q of 45.7 CFM was calculated. This value was plotted on the blower performance curve shown in figure 3.4 to find the static pressure output. For 45.7 CFM, this correlated to a static pressure output of about 361.3 Pa. The next step was to determine the system constant, K, which represented the resistance of the entire blowing rig system to prevent flow from passing through it. For this experiment, the system curve used is given by equation 3.2.

$$P = \frac{1}{2}KQ^2 \tag{3.2}$$

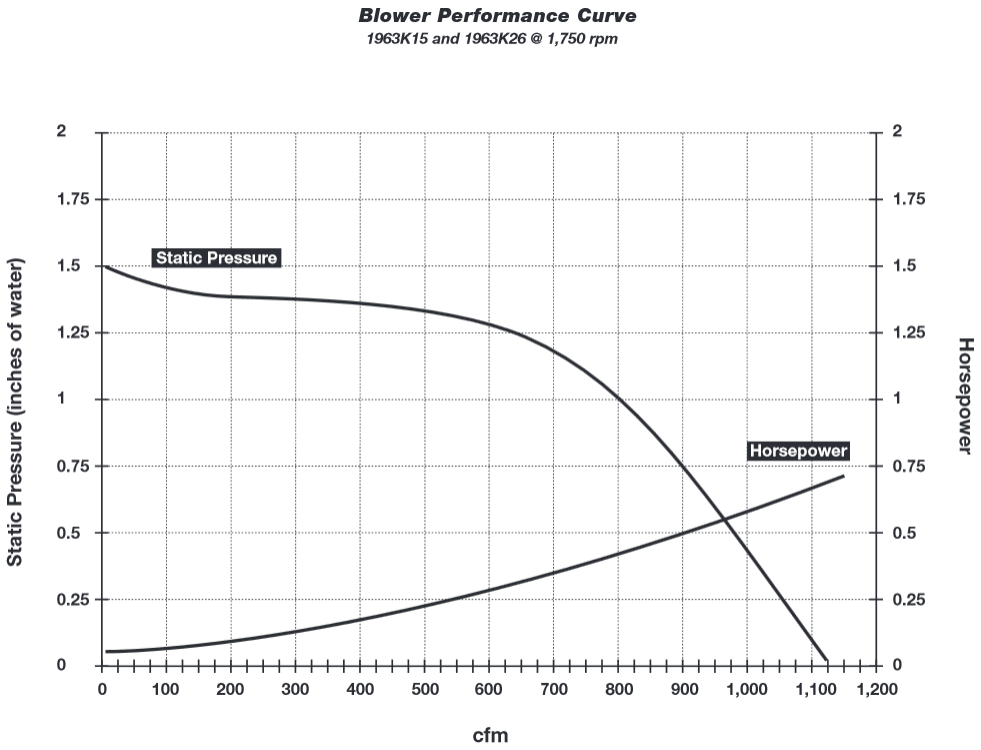

Figure 3.4: Blower performance curve, taken from www.mcmaster.com

Solving eq. 3.2 for K resulted in a system constant of 0.0014 inH_2O/cfm^2. Plotting the resulting system curve represented by equation 3.2 onto the blower fan curve, as shown in figure 3.4 made it possible to determine the required P to produce the needed Q for a 1% BR. For this experiment, the design point was to produce a 1% BR for a U_b of 10 m/s which was the bulk velocity determined by PIV at the test section. For a BR of 1%, the required Q was found to be 215 CFM. Inputting that value into the current system curve resulted in a P of 32.36 inH_2O, or about 8 kPa. From that result, it was obvious that the current blower and/or blowing rig configuration was insufficient in producing the needed flow injection. To overcome this obstacle, it was determined that the easiest step was to modify the blowing rig to reduce the system resistance. These modifications consisted of removing current ductwork connecting the blower outlet to the top of the blowing rig and replacing it with a shorter length, larger diameter duct. The new duct hose was a highly flexible,

PVC coated fiberglass material with a 15.24 cm inner diameter (McMaster-Carr part number 5501K65). This new hose was connected to a larger blower reducer which could fit with the 15.24 cm diameter. Since the hose was highly flexible, there needed to be a fixed joint at the other end of the hose to feed into the top of the blowing rig. A 15.24 cm inner diameter PVC coupling was chosen to connect the other end of the hose (Charlotte Pipe model number PVC 00100 1600). The hose was connected to the coupling by applying duct tape to the inside of it and the edge of the hose. The coupling also served as a mount for Pitot tubes that were used to measure the flow rate which will be discussed in section 3.5. To connect the coupling to the top of the blowing rig, the current hole at the top of the diffuser had to be widened enough so the that coupling could fit. This fitting proved to be a sufficient seal which meant no further connections had to be made to hold the coupling in place. After determining the new system curve with the updated blowing rig, it was found that current blower could produce the required 1% BR. Applying this configuration to the new extended blowing rig allowed for a slight increase in BR due to the smaller inner injected area of 0.96 m^2 per section. This meant that an additional three blowers had to be purchased so that each section could have a dedicated blower.

To maintain fully developed conditions, it was then necessary to prevent the injected mass flux from increasing the net mass flux through the channel. This meant that as the flow was being injected into the channel, it also needed to be suctioned out at the same rate. The approach taken was to change the bottom surface of the channel which was smooth and impermeable, to one that was smooth and porous. The same perforated PVC material used to mount the rough surface was again used to act as the suction surface. To make the surface smooth, a thin sheet of fabric was glued to the channel facing side. The fabric was carefully applied to ensure that no wrinkles and other non-uniformities could disturb the flow. To suction the flow through the surface, the intake of each of the blowers were utilized. This meant that all of the

blowers had to be contained within a sealed volume of air that covered the full length of the suctioned surface. This would allow the blowers to pull air from inside the channel. The method to accomplish this was to seal each of the blowers within an enclosure that would be durable enough to withstand the pressures of the channel at high speeds. The enclosure itself was made from 3.5 mil clear polyethylene sheets. The sheets were then wrapped around a PVC structure made from 1 inch diameter pipes which served as a skeleton to support the enclosure. This PVC structure covered a volume equal to the full suctioned area of the channel extended down to the floor. Duct tape was used to secure the edges of the bag to the walls of the channel and create an airtight seal. The duct hose connecting each blower exit to the top of the diffuser was allowed to come out of the enclosure and wrap up around the side of the blowing rig. The openings in the bag made from the hoses were sealed up around each hose using duct tape.

The final modification that needed to be made was to allow optical access at the test section for the PIV system. This meant that the vertical walls of the channel at the test section needed to be transparent to allow the PIV cameras to observe the flow. It was determined that clear, polycarbonate panels with dimensions of $0.5 \times 4.0 \times 72.0$ cubic inches would be used (McMaster-Carr part number 1749K649). These panels were drilled, tapped, and then fastened to the perforated PVC using 1/4-20 bolts. A schematic of the final section of the wind tunnel is provided in fig. 3.5

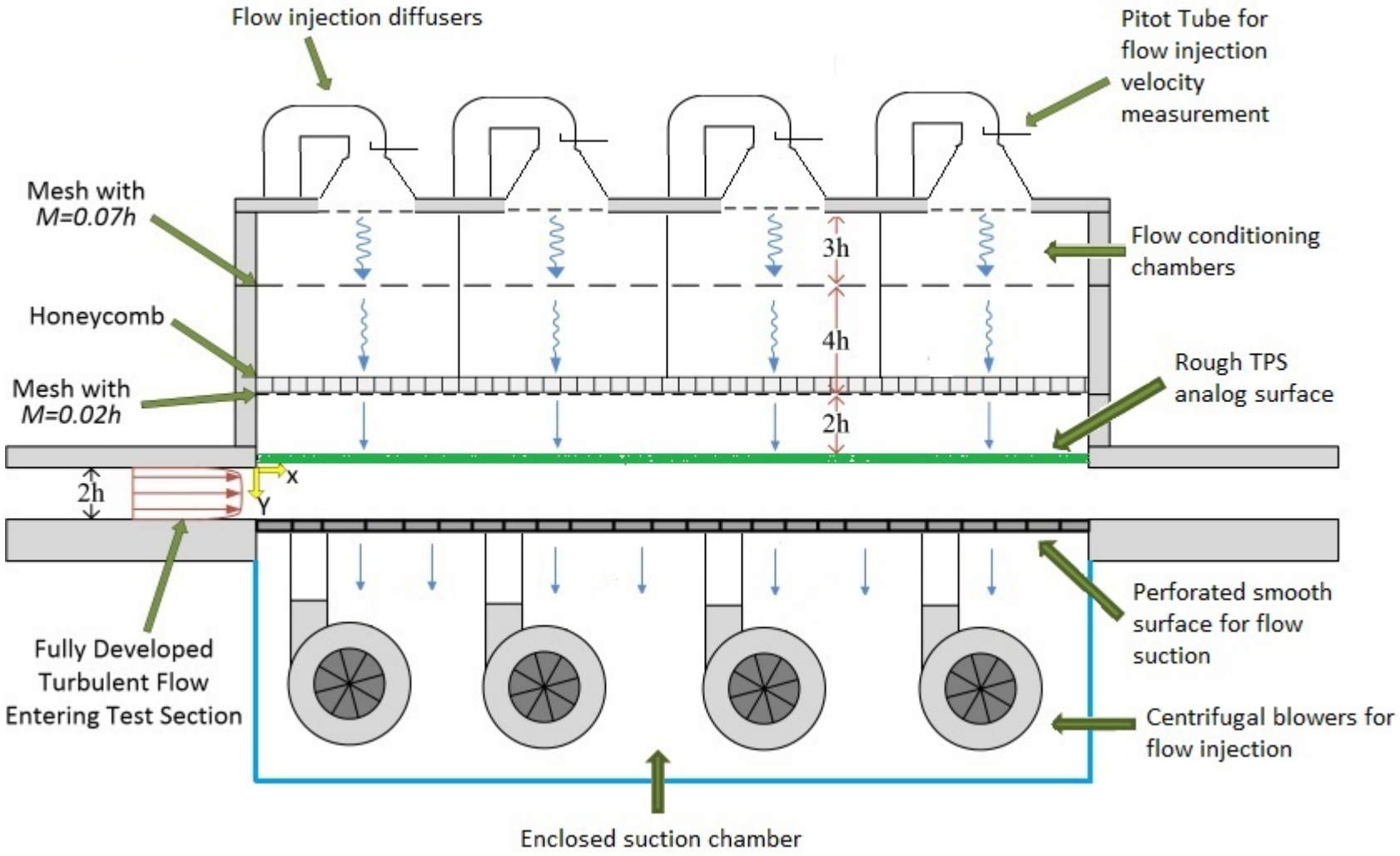

Figure 3.5: Schematic of the final blowing rig design used in the experiment.

3.3 Particle Image Velocimetry

In this experiment, all quantities needed to measure τ_w as in equation 2.42, other than V_0, were found using PIV. This measurement technique consists of seeding a given flow field using small particulates such as aerosols. These particulates are then illuminated in a plane using a laser, at which time images are recorded in quick succession. A analysis of the images are conducted to find locally-averaged particle displacements between two images separated by short time displacement and hence, a velocity vector field. PIV offered several advantages for this research as it is non-intrusive, is able to measure spatially distributed flow fields, and can measure multiple components of velocity simultaneously. Here, a high speed PIV system manufactured by LaVision GmbH was used. The basic system consists of a high speed digital camera, laser, optics, timing hardware and image analysis software. In these measurements an optical arrangement was used which captured the streamwise and wall-normal components of velocity.

Particle images were captured using a single Phantom Miro M310 high-speed digital camera. Images were digitized using a CMOS sensor. The camera featured a 1280 $\times$ 800 maximum resolution with a 20 μm pixel size and 12-bit pixel depth. It also featured a throughput of 3.2 Gigapixels/second which translated to a frame rate of 3200 fps. This frame rate could be increased to 650,000 for reduced resolutions. Attached to the camera was an AF Micro-Nikkor lens. This lens had a focal length of 200 mm with a minimum $f^{\#}$ of 6.25 and maximum of 50. The camera was aligned and focused to capture the images within the laser sheet near the centerline of the channel.

The laser used in this experiment was a Litron LDY302 model. This laser was specifically designed for use in PIV experiments and featured two continuous wave Q-switched Nd:YLF DPSS laser resonators that produced infrared light at 1053 nm

wavelength. This light is converted to visible green light at 527 nm by an intra-cavity Harmonic Generation Assembly (HGA). Output energies up to 30 mJ at a 1 kHz repetition rate and 5 mm beam diameter were possible. The two lasers are independently controlled and pulsed which allowed for a double pulse output with inter-pulse separation times of < 10 ns. This gave the dual laser system an advantage over a single laser system in it's ability to achieve the ultra-short pulse separation. This advantage was utilized in the experiment to capture PIV images at high frame rates for flow conditions that were too large for the single-pulsed setting to resolve the velocity components. The laser was powered by an external 50 Hz single-phase 220 VAC supply which contained a water-to-air chiller unit used to cool the laser diodes and rods during operation.

The optics set used in this experiment was a LaVision model 1108405. The divergence lens used had a focal length of 20 mm and produced a sheet thickness that could be adjusted from 0.5 mm - 2.5 mm. There was some initial difficulty in determining the optimal location to position the optics. It was originally planned to position the optics directly underneath of the channel. Due to the presence of the suction surface enclosure and the constant need to ensure that the sheet was properly focused, keeping the optics underneath would have required significant modification to the blowing and suction apparatus. It would have also been necessary introduce a slit within the perforated PVC to allow for the light sheet to pass through into the channel. This could have possibly introduced instabilities within the flow at the test section. Instead, the light sheet was introduced through the outlet of the wind tunnel using optics mounted to a small optical table which was situated on top of the exit section of the channel. Using two Thor Labs BB1-E02 broadband dielectric mirrors, the laser could be reflected and directed into the lens. One of the mirrors was mounted to an adjustable rail and placed on the floor, the other was mounted directly to the optics system via a Thor Labs thread adapter. A diagram of the optical setup

and PIV laser orientation can be seen in figure 3.6.

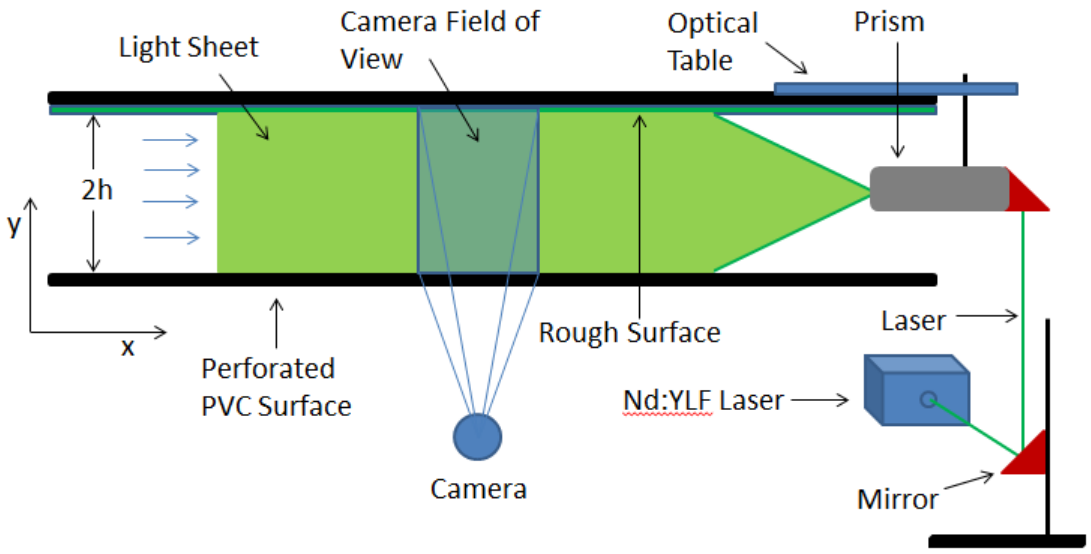

Figure 3.6: Diagram of optical setup and laser orientation.

To seed the flow with particles, a LaVision model 1108926 aerosol generator was used. The seeding fluid was Di-Ethyl-Hexyl-Sebacat (DEHS) which is commonly used to generate steady aerosols. The DEHS was loaded into the reservoir connected to the generator body. The generator itself operated at a maximum working pressure 600 kPa. This pressure was provided by a compressed air source located within the lab which was connected via hose to the generator inlet. The seeding amount that was injected into the flow could be varied using a pressure reducer that was controlled by knob located on the top of the generator. The 19 mm diameter outlet of the generator was connected to another hose which was fed into the inlet of the channel blower. The generator was originally placed at the beginning of the flow injection section of the channel. This location proved to be ineffective in evenly distributing the aerosol particles which was seen in preliminary images at the test section.

The entire PIV system was controlled by a LaVision model 1108075 High Speed Controller (HSC). The HSC was capable of producing complex patterns of pulses with accurate timing between multiple outputs for up to 16 different channels. The HSC was designed to work with LaVision's image acquisition and processing software called

DaVis. The user defined pulse widths and intervals between pulses were automatically programmed by DaVis.

All images in this experiment were taken using the double-frame/double-exposure mode. In this mode, two images were recorded from two different exposures that were separated by a time dt. This dt was determined to be of optimal length such that an average particle shift of 5 pixels was seen between images [49]. Due to the wide range of tunnel speeds investigated, the dt had to be adjusted and was optimized before each run.

3.4 Rough Surface Characterization

This experiment focused on the modification of τ_w over an ablative TPS analog surface. Ideally, an actual TPS surface such as the Phnenolic Impregnated Carbon Abalator (PICA) would be used. Due to ITAR restrictions however, a surface geometrically similar to PICA had to be used instead. It was originally planned to use a material called $Fiberform^{TM}$ for the rough surface which forms the carbon matrix for PICA. This surface was discussed in the work by Lachaud and Mansour [50]. The Fiberform was used in preliminary investigations for the work in this thesis to determine its ability to be subjected to flow injection. While the surface was porous enough to allow for flow injection, it proved to be insufficient to achieve the required blowing rates. Furthermore, the roughness height was relatively small, so that the Reynolds numbers required to achieve fully rough conditions in the existing wind tunnel were significantly higher than could be expected during re-entry. This, on top of it's relative high cost and fragile nature meant that an alternative surface had to be found. It was determined that a scaled TPS analog surface similar to heavy duty scouring pads would provide sufficient geometric similarity, with much higher roughness heights. The actual material used in this experiment was made from synthetic fiber woven into mesh tiles with dimensions of $22.86 \times 15.24 \times 1.27$ cm^3. These tiles

were mounted onto the perforated PVC inside of the blowing rig and arranged so that the edge of the surface would be flush with the top of the inner channel wall.

It was then necessary to characterize the surface so that a quantitative comparison with the $Fiberform^{TM}$ surface could be made. Due to the complex geometries found in surface roughness as discussed in the previous chapter, various methods have been employed by researchers to characterize it. A common method is through measuring roughness height distributions. In a recent work by Wilder and Reda [4], roughness height distributions were measured for sphere cone ballistic models that were inspired by actual re-entry vehicles. These models were grit-blasted with aluminum oxide particles to produce the roughened surface. Using a technique called confocal microscopy, it was possible to produce 3D surface elevation maps of selected regions of the models. A topographical analysis was then performed on the maps to identify the individual roughness elements [51]. An example of the roughness elevation maps can be seen in fig. 3.7.

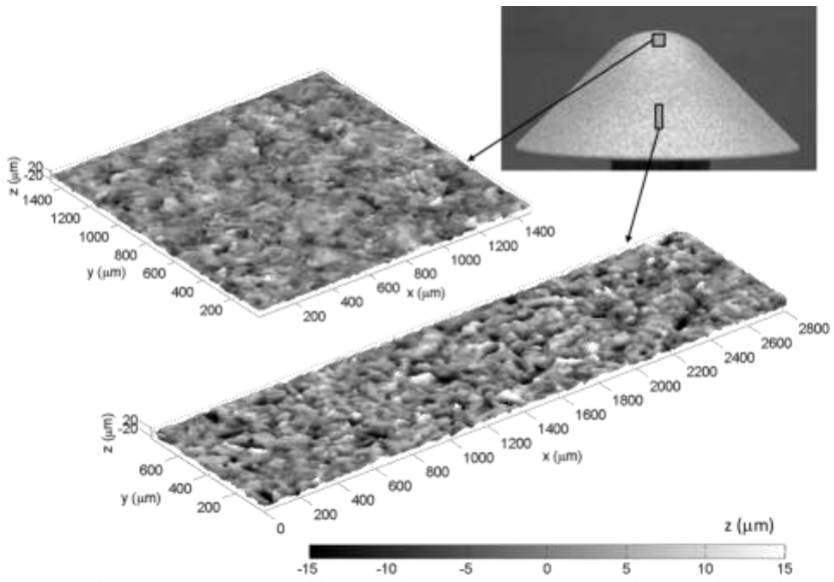

Figure 3.7: Roughness elevation maps from the nose and frustum of sphere cone models used in [4].

Due to the large variation in roughness heights in the TPS analog, a slightly different

approach had to be taken to characterize the TPS analog surface. It was determined that roughness heights could be measured by optically capturing profiles of the tiles and analyzing them through the use of image processing software. This process did not produce 3D surface maps which meant that the actual peak-to-valley element heights could not be calculated. Instead, a statistical approach was used analyze the surface. Using a Nikon D500 digital camera and a 200 mm macro lens, a series of images of 20 different tiles were taken at 3 distances of 12.7, 25.4, and 38.1 cm away from the surface. These images were uploaded into Matlab and were first converted to a grayscale image. They were then converted to a binary image which showed the roughness elements that could be measured. A side-by-side comparison of the original and binary images can be seen in fig. 3.8. From the binary images, it was

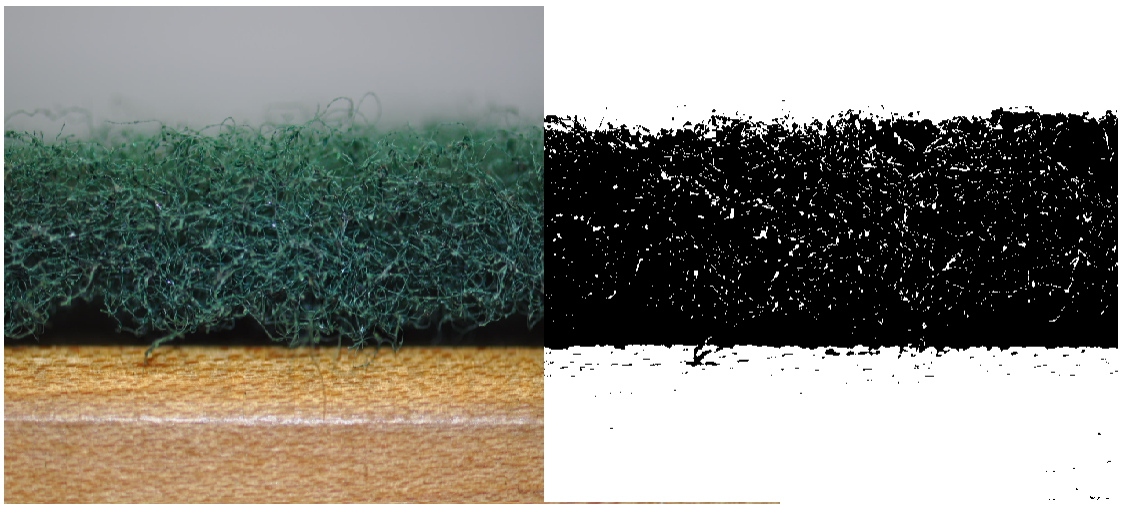

Figure 3.8: Comparison of original and binary images at the 5 inch distance.

possible to extract roughness heights by determining the number of pixels in each element. By referencing the number against a zero and using a scaled image for each distance, the number could be converted to a physical dimension. The scaled image consisted of a ruler focused on the plane of the tile edge. Compiling the roughness heights and non-dimensionalizing them by the root mean square, it was possible to calculate normal probability density functions shown in fig. 3.9 using the

mean of the non-dimensional heights, k/k_{rms}. To form a basis of comparison, stylus

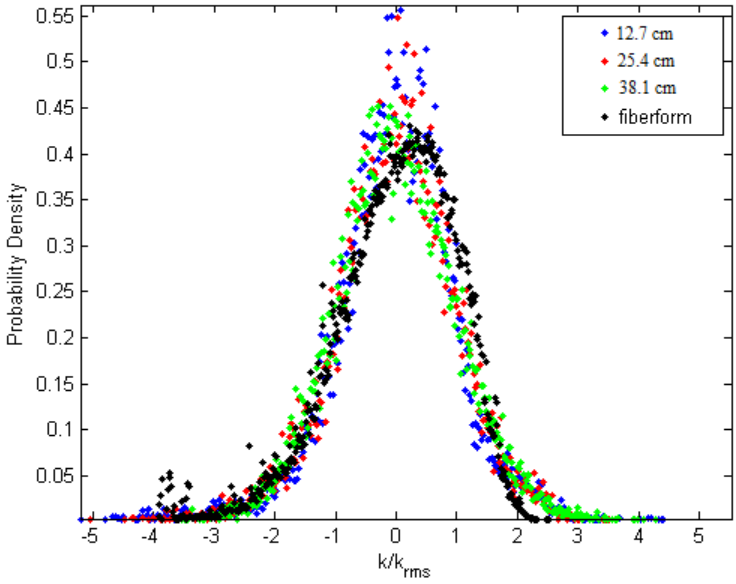

Figure 3.9: Probaility density functions for the analog surface at each measurement length and $Fiberform^{TM}$.

surface profilometry data taken from $Fiberform^{TM}$ samples were used. This data was also used to calculate a probability density function and was plotted alongside the other results in figure 3.9. Overall, each of the roughness distributions are nearly uniform with a slight skewness. This differs from other roughness investigations where the sample distributions were found to be non-uniform [52], [53]. The 12.7 cm and 25.4 cm distributions were negatively skewed having a skewness of -0.473 and -0.301 respectively whereas the 38.1 cm distance resulted in a skewness of 0.067. The $Fiberform^{TM}$ had a skewness of -0.745. These results show that the analog surface is comparable to the $Fiberform^{TM}$. More specifically, this meant that the two surfaces are similar enough that the k_{rms} value can be used to scale the Reynolds number to compare current results with future $Fiberform^{TM}$ measurements.

3.5 Flow Injection Measurement

The bulk of this experiment was heavily dependent on accurately measuring the BR in order to show the modification to τ_w due to blowing. This meant that there needed to be a reliable method to measure V_0 for the injected flow out of the rough surface and into the channel. It was initially assumed that V_0 would be measured directly via the PIV system. In this case, V_0 would come from the measured value of $\langle V \rangle$ at the test section. According to theory, this value should remain constant across the channel. After processing the images taken by the high-speed cameras at the test section, it was found that the magnitude of $\langle V \rangle$ could not be resolved with sufficient accuracy as it was within the expected uncertainty of the PIV measurement approach. Another issue with this approach was that the BR had to be set before each test run. This required that images had to be taken and processed before the actual test data could be gathered. This would have proved to be a time consuming and inefficient method if the BR was incorrect with first set of images. This meant that another method was needed to measure V_0.

The next approach taken was to apply a control volume analysis to the blowing rig section from the 15.24 cm diameter PVC inlet to the section of rough surface at the exit of the blowing rig. A diagram of this volume is seen in fig. 3.10. By utilizing conservation of mass, and measuring the velocity of the flow at the PVC inlet using a Pitot tube, V_0 can be found indirectly through the change in surface area assuming constant density. This is represented by

$$V_0 = \frac{U_1 A_1}{A_2} \tag{3.3}$$

where U_1 and A_1 is velocity of the flow and area respectively at the PVC inlet. A_2 represents the area of the section of rough surface at the exit of the blowing rig. The areas of both surfaces are well defined with $A_1 = 0.0182m^2$ being the area of a circle

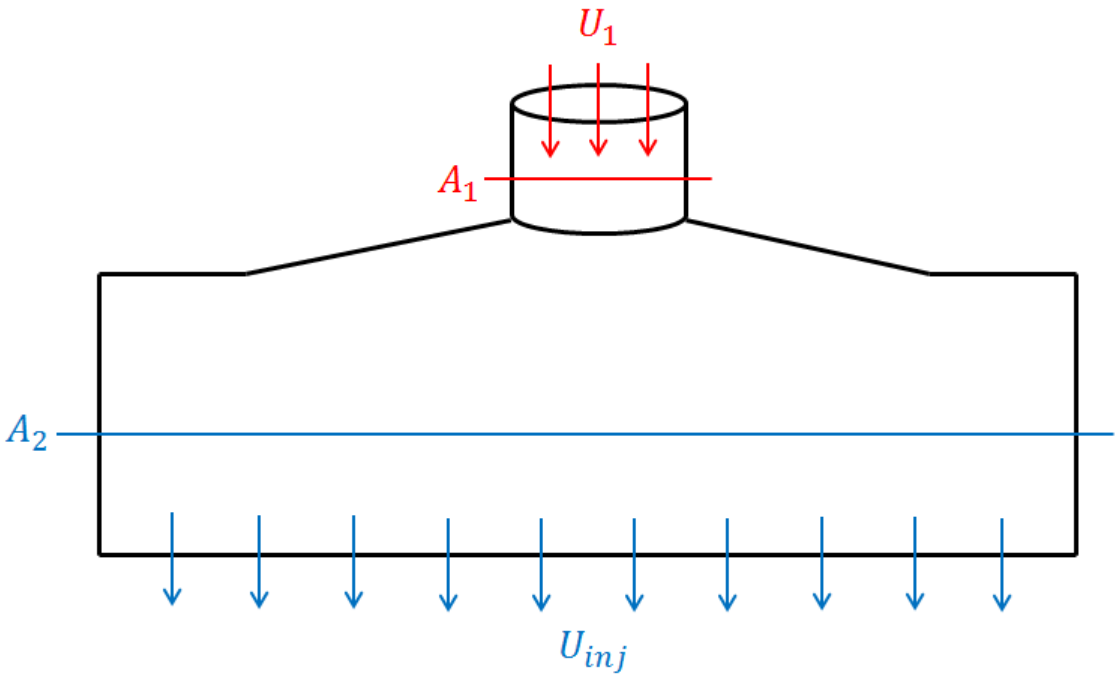

Figure 3.10: Diagram of the volume used to determine V_0.

with diameter of 15.24 cm and $A_2 = 0.9581\ m^2$. The difficulty with this approach was the accurate measurement of U_1. In this analysis, U_1 represents the area-averaged velocity of the flow through the cylindrical PVC coupling. The area-averaged velocity is given by

$$U_1 = \frac{1}{\pi R^2} \int_0^{2\pi} \int_0^R U(r) r dr d\theta \tag{3.4}$$

where R is the coupling radius of 0.762 m, and $U(r)$ represents the measured velocity at the radial distance r from the center. It was assumed that given the shape of the duct hose as it bent around to the top of blowing rig, that the flow would be symmetric inside of the coupling about the axis parallel to the plane of the bend. The area-averaged velocity was then found by measuring the velocity profile along that axis and integrating along the asymmetric halves. This can be represented as a modified form of eq. 3.4

$$U_1 \approx \frac{1}{\pi R^2} \left[\pi \int_0^R U(r) r dr_{\ half1} + \pi \int_0^R U(r) r dr_{\ half2} \right] \tag{3.5}$$

The velocity profile inside of the coupling was measured using a Dwyer Instruments Pitot-static tube with a 0.318 cm diameter and 30.48 cm insertion length. The tube was mounted on the coupling by drilling and tapping into the PVC to allow for the 0.318 cm MNPT fitting. With the tube mounted into the coupling, it was possible to manually traverse the tube across the diameter to obtain the velocity profile. It was determined that since similar materials and dimensions were used for each section in the blowing rig, that the velocity profile of only one section had to be measured which could then be applied to the other sections.

The experimental procedure to measure the velocity profile involved dividing up the Pitot-static tube into 1.27 cm increments. These increments were marked onto the tube using a ruler and permanent marker. To acquire the pressure measurement at each increment, an Omega 0.5 in.H_2O pressure transducer (model #: PX653-05D5V) was used. The actual voltage output was read using a multimeter and an average reading was recorded at each increment. Across the 15.24 cm diameter coupling, a series of 13 average voltages were recorded to make up the complete profile. These voltages were first converted to pressures and then to velocities using Bernoulli's equation. The complete velocity profile can be seen in fig. 3.11 which has been referenced from the center of the coupling. This resulted in $U_1 = 6.94$ m/s. To remove the need to measure profiles during every test run, it was determined that a single measurement at the center would be used. This center measurement would then be corrected to account for the difference in velocities between the center and area-averaged velocity. This correction factor, c, was found using

$$c = \frac{U_1}{U_{center}} = 0.9929. \tag{3.6}$$

This factor was then used to determine the needed measured velocities for a given BR which will be discussed in the next section.

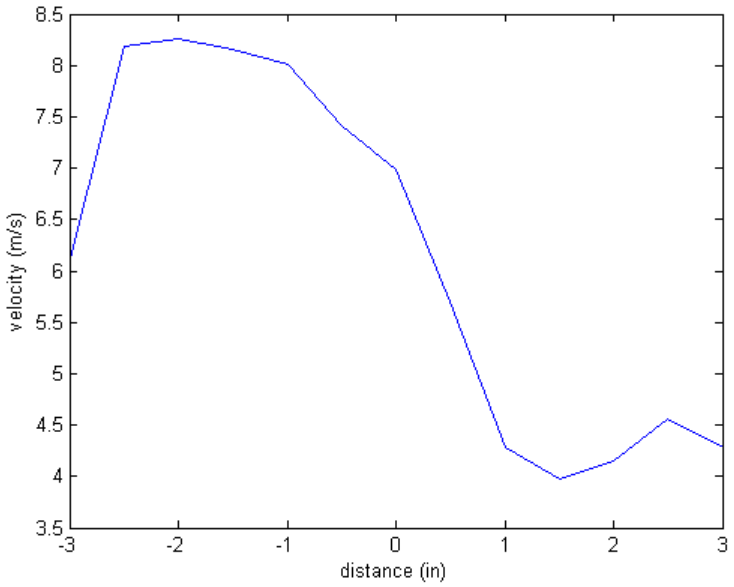

Figure 3.11: Velocity profile across the inside of the PVC coupling.

3.6 Measurement Procedures

The objective of this thesis was to examine the modification of τ_w of a TPS analog surface due to the effects of suction and blowing. This meant that in order to obtain a clear enough picture of these effects, a wide range of channel speeds and BR had to be tested. This resulted in utilizing the channel and blowing rig's performance capabilities to the greatest extent possible. From preliminary test runs, it was found that the entire blowing rig's structural integrity began to fail at the wind tunnel motor controller's frequency of 55 Hz. It was also observed through analysis of the pressure gradient throughout the channel that the flow was not fully developed at a frequency of 5 Hz. As a result, it was decided that the test range would be between 10 Hz and 50 Hz which corresponded to U_b of 2.834 m/s and 13.134 m/s respectively .

The test runs were split up into two groups consisting of runs where there was no flow injection (non-blowing) and runs with flow injection (blowing). The non-blowing cases were collected first followed by the blowing cases. For the blowing cases, each

BR was tested at that particular tunnel frequency before the frequency was changed. Table 3.1 gives the full range of flow conditions that were tested. The sample times shown in table 3.1 were determined based on the premise that ∼1000 statistically independent samples were needed of the largest eddies in the flow. This quantity provided a statistically converged average of the flow effects due to these eddies. From previous studies on channel flow, it has been shown that the largest eddies are about $20h$ [54–56]. For the channel used in this experiment with $h = 50.8$ mm, this meant that the largest eddies encountered would be ~ 0.1 m. In order to capture 1000 independent samples, around 100 m of flow had to be measured. This 100 m guideline was multiplied by U_b, which was found through the pressure difference encountered at the contraction section of the channel, to determine the sample time needed for each run. The sample time was used to adjust the camera's image rate so that the 1000 samples could be evenly distributed about the 100 m of flow. The camera's memory was capable of storing a little over 4000 images. This meant that in the vector calculations, a single statistically independent sample was contained within every 4 images.

The measurement procedure for the non-blowing cases was fairly straightforward. To begin, the channel was set to the desired blower frequency and the aerosol generator was turned on. At this point, it was necessary to ensure that the flow had a proper seeding density and pixel shift. This was accomplished by capturing a preliminary series of images. The amount of seeding was then adjusted if needed along with the dt between images if the pixel shift was undesirable as mentioned in section 3.3. Once the flow was allowed to stabilize, the data set was captured and stored to the computer's hard drive for future analysis.

The procedure for the blowing cases was more complicated. After ensuring proper flow seeding and pixel shift, it was necessary to set the desired BR. Using U_b, which was calculated from the PIV images for the non-blowing cases, a spreadsheet was

created to determine the needed V_0. This process consisted of working backwards starting with U_b and calculating V_0 using the BR for the desired case as in equation 3.1. From V_0, U_1 could then be found using equation 3.3. U_1 was then corrected using c to obtain U_{center} which was the velocity that would need to be measured by the mounted Pitot-static tubes in the PVC couplings. This would then be used with

$$\Delta E = \frac{\rho U_{center}^2}{2S} \tag{3.7}$$

where ΔE is the voltage difference needed to obtain the correct BR and S is the span of the pressure transducer in Pa/V. The same Omega 0.5in.H_2O pressure transducer was used to measure ΔE as in the preliminary BR investigations discussed in section 3.5. This transducer was connected to a digital monitor which allowed for a real-time display of the voltage measured. This was needed in order to tune the blowers to the proper output. To tune each blower, a 15 A VenTech variable speed controller was connected in line with wall power supply. Since there was only one pressure transducer available, each blower had to be tuned independently before the data collection could begin. To tune each blower, the dial on the speed controller was adjusted until the digital readout consistently stayed within ± 0.005 V of the desired ΔE for a period of 10 seconds. After each blower had been tuned, the flow was allowed to stabilize to account for the added injected flow within the blowing rig upon which time the data was then collected and stored.

The first step in calculating the velocity vectors was to pre-process each of the images. This consisted of first masking out both the suction and rough surfaces from the images in order to prevent the software from taking these features into account in the analysis. Next, an image inversion was conducted which improved the contrast between the particle and background intensities. A calibration image also had to be taken. This was accomplished by taking an image of a meter stick along the same

plane as the light sheet. An example of one of the calibration images used can be seen in fig. 3.12. The images were scaled by selecting two horizontal points as seen by 1 and 2 in fig. 3.12. By inputting the corresponding length associated with the selected points, the images could then be converted to physical dimensions. The resulting velocity components were in units of m/s for this experiment.

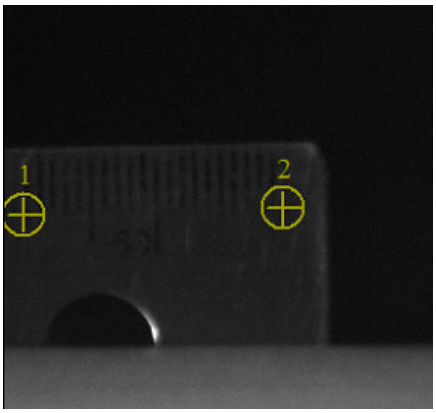

Figure 3.12: PIV calibration image.

The velocity components were calculated using a cross-correlation method in which two images were subdivided into square 64 x 64 pixel^2 interrogation windows. Each window was then shifted between the images by varying distances to identify the most likely particle-image pair displacement. This was represented by the highest peak in the cross-correlation function. A more in depth discussion can be found in [57–59]. Neighboring interrogation windows were offset with a 75% overlap which meant that the 1280 x 800 pixel^2 resulted in a grid of 26 x 16 interrogation windows and 416 vectors for each image pair. The vector field was calculated using a constant size multi-pass option of 5 iterations. In the initial pass, a vector for each interrogation window was processed. This vector was then used as a reference for the next pass after the interrogation window according to the determined particle image shift. This technique helped to improve the signal-to-noise ratio and resulted in more accurate vectors.

Table 3.1: All test conditions

Case	U_{cl} (m/s)	$Re = U_b h/\nu$	BR (%)	Sample Time (s)	Image Rate (kHz)
1	3.36	20000	0	29.8	0.165
2	3.36	20000	0.25	29.8	0.165
3	3.36	20000	0.5	29.8	0.165
4	3.36	20000	0.75	29.8	0.165
5	3.36	20000	0.98	29.8	0.165
6	5.52	31000	0	18.1	0.2
7	7.86	41000	0	12.7	0.4
8	7.86	41000	0.25	12.7	0.4
9	7.86	41000	0.5	12.7	0.4
10	7.86	41000	0.75	12.7	0.4
11	7.86	41000	0.98	12.7	0.4
12	10.09	49000	0	9.9	0.41
13	12.32	57000	0	8.1	0.5
14	12.32	57000	0.25	8.1	0.5
15	12.32	57000	0.5	8.1	0.5
16	12.32	57000	0.75	8.1	0.5
17	12.32	57000	0.98	8.1	0.5
18	14.6	67000	0	6.8	0.6
19	16.86	75000	0	5.9	0.66
20	16.86	75000	0.25	5.9	0.66
21	16.86	75000	0.5	5.9	0.66
22	16.86	75000	0.75	5.9	0.66
23	16.86	75000	0.98	5.9	0.66
24	18.93	83000	0	5.3	0.75
25	21.31	92000	0	4.7	0.85
26	21.31	92000	0.25	4.7	0.85
27	21.31	92000	0.5	4.7	0.85
28	21.31	92000	0.75	4.7	0.85
29	21.31	92000	0.98	4.7	0.85

Chapter 4 Results and Discussion

The primary objective of the analysis in this thesis was to determine τ_w. The DaVis software was capable of calculating the wall-normal, V, and streamwise, U, components of velocity along with the relevant turbulence statistics needed to determine τ_w. These values were averaged across the entire range of PIV images for each case and further averaged in x in order to produce wall-normal profiles for each of the values. The results are organized into four different sections. Section 4.1 focuses on the each of the statistics that were involved in calculating τ_w including the mean velocity profiles and mean Reynolds stress profiles. Section 4.2 focuses on the shear stress measurements at each point across the height of the channel. Section 4.3 discusses the modification of τ_w due to roughness and blowing effects. Finally, section 4.4 deals with the validation of the τ_w measurements.

4.1 Overview of Mean Statistics

The statistics required to determine τ_w included the streamwise velocity gradient $\frac{d\langle U\rangle}{dy}$ which depended upon the mean streamwise velocity component $\langle U\rangle$. The mean wall-normal velocity component $\langle V\rangle$ was of interest to use as a cross-reference for the measurement of V_0 which was assumed to remain constant in the y-direction across the channel (see derivation of eq. 2.32). The mean components of the Reynolds stress tensor $\langle u'v'\rangle$, $\langle v'^2\rangle$, and $\langle u'^2\rangle$ were needed not only to calculate τ_w but to also gain insight into the turbulence structure and generation.

The vector field images calculated by the PIV software produced an x, y field of

different statistics of interest. For an arbitrary time averaged statistic $\overline{\phi}(x,y)$, $\langle\phi\rangle(y)$ was found through

$$\langle\phi\rangle(y) = \frac{1}{n}\sum_{i=1}^{n}\overline{\phi}_i(x,y) \tag{4.1}$$

where n is the number of samples in each x-direction row of the time-averaged statistic field $\overline{\phi}_i(x,y)$. The region used to calculate $\langle\phi\rangle$ could be tailored for each image to account for errors introduced at the edges of the fields caused by particles entering and leaving the images between the acquisition of image pairs.

The $\langle U\rangle$ and $\langle V\rangle$ profiles were non-dimensionalized by the bulk streamwise velocity U_b which here is defined by

$$U_b = \frac{1}{2h}\int_0^{2h}\langle U\rangle(y)dy. \tag{4.2}$$

This bulk velocity is able to account to for any slight asymmetry in the mean velocity profile which was induced by the roughness and/or blowing effects. The wall-normal position y was also non-dimensionalized by h with the zero position referring to the location of the rough wall. For the Reynolds stress profiles, the $\langle u'v'\rangle$, $\langle v'^2\rangle$, and $\langle u'^2\rangle$ components were non-dimensionalized by U_b^2.

4.1.1 Non-Blowing Cases

The full-range of mean velocity profiles of $\langle U\rangle$ and $\langle V\rangle$ for the non-blowing cases can be seen in fig. 4.1 and 4.2. The full-range of profiles for the mean components of the Reynolds stress tensor $\langle u'v'\rangle$, $\langle v'^2\rangle$, and $\langle u'^2\rangle$ for all non-blowing can be seen in fig. 4.4, 4.5, and 4.3 respectively. Each of the curves represent a single test case at the specified Reynolds number. The corresponding flow parameters can be seen in table 3.1.

Looking at fig. 4.1, it is evident at the lower Re that the flow shows signs of not being fully developed due to the slight asymmetry in the shape of the profile. As

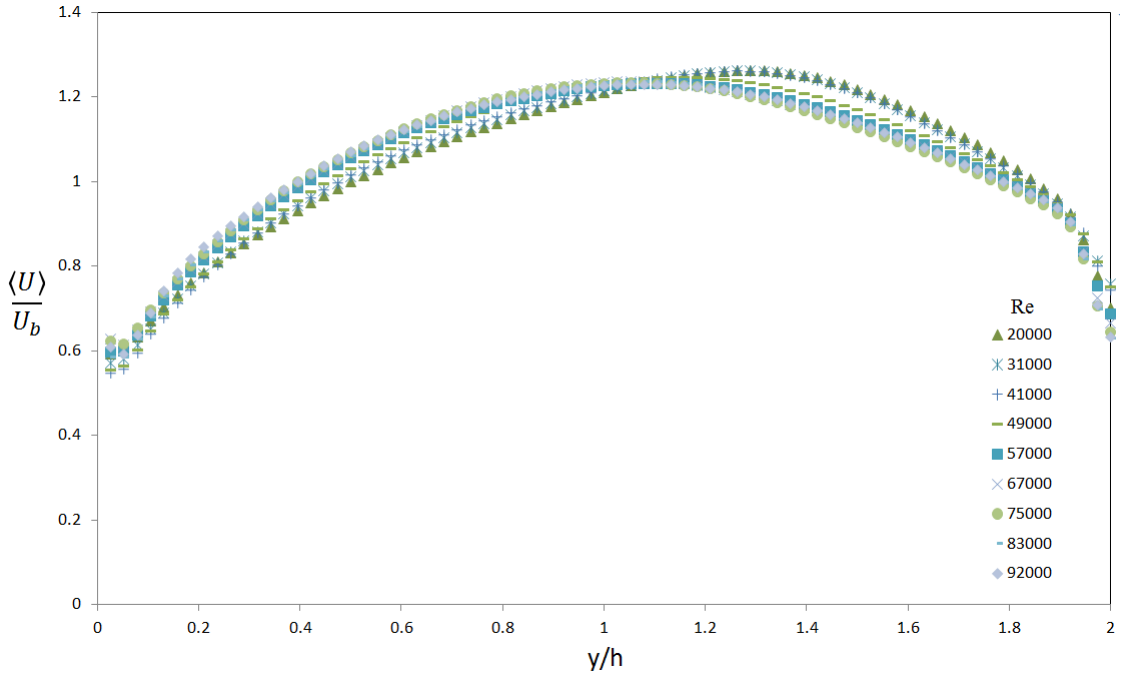

Figure 4.1: Full range of mean streamwise velocity profiles for all non-blowing cases.

Re is increased however, the profiles begin to collapse. The location of maximum velocity shifts from about $1.3h$ near the smooth wall for lower tunnel speeds, to near the centerline at around $1.1h$ for the higher speeds.

According to eq. 2.32, $\langle V \rangle$ should remain constant at V_0 across the height of the channel and, for the non-blowing cases, should remain zero. It can be seen in fig. 4.2 that there exists a slight $\langle V \rangle$ equal to approximately $0.015U_b$ in the case of non-blowing. It was concluded that this slight velocity was within the expected level of experimental error. This error could have come from a slight coordinate system rotation relative to the wall due to camera misalignment. A rotation of less than 1 degree would result in a 1.5% shift of the streamwise velocity component into the wall-normal component. In each of the cases, the velocity measured remains constant across the height of the channel with maximum fluctuations of around $\pm 0.005U_b$.

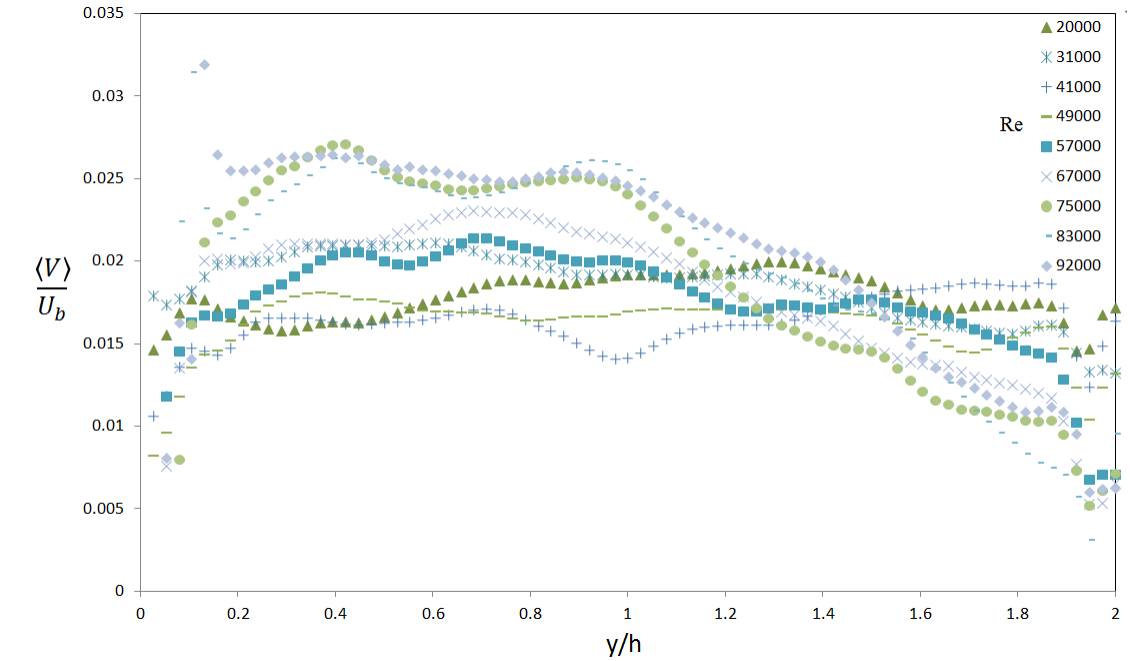

Figure 4.2: Full range of mean wall-normal velocity profiles for all non-blowing cases.

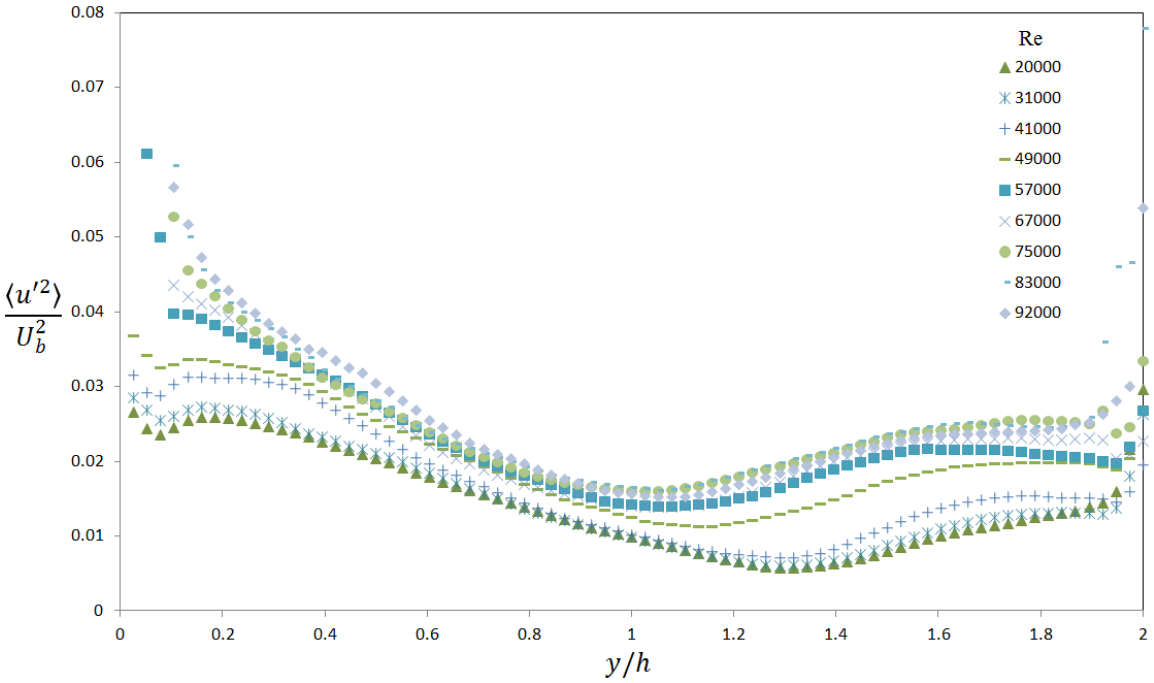

Figure 4.3: Full range of $\langle u'^2 \rangle$ profiles for all non-blowing cases.

The full range of $\langle u'^2 \rangle$ profiles for all non-blowing cases is shown in fig. 4.3. The variance of the streamwise velocity fluctuations gives insight into where the majority

of the turbulence is being generated. As expected, the increase in Reynolds number causes an increase in turbulent kinetic energy. This effect is greater near the walls where the flow is bounded and the shear stress acts to generate the turbulence. The point of minimum $\langle u'^2 \rangle$ also shifts from $1.3h$ for the lower Reynolds numbers to near the centerline for greater cases.

Looking at fig. 4.4, as expected, as Re is increased, the magnitude of $\langle u'v' \rangle$ increases as well. An interesting feature to note is that each of the profiles appear to pivot at about the $0.7h$ location near the rough wall. This could possibly be due to the asymmetry of the channel geometry with the rough and smooth walls. While there was a relatively large amount of data scatter near each of the walls, the smooth wall appears to have little effect on $\langle u'v' \rangle$ in contrast to the rough wall in which the profiles differ at that location with each Reynolds number. The linearity seen in the profiles was predicted by eq. 2.42 where the Reynolds shear stress ($\rho \langle u'v' \rangle$) term contributes the most to the overall τ in the outer layer compared to the viscous shear stress $\left(\rho \nu \frac{d\langle U \rangle}{dy} \right)$ term which only becomes relevant near the walls.

The full range of $\langle v'^2 \rangle$ profiles for all non-blowing cases is shown in fig. 4.5. The profiles show magnitudes of $\langle v'^2 \rangle$ with rms values at around 6% of U_b for lower Re cases up to around 10% of U_b for the higher cases. It is expected that $\langle v'^2 \rangle$ will be much higher than $\langle V \rangle$ in wall-bounded flow due to the anisotropic shear generation at the larger scales of turbulence. Compared to the $\langle u'^2 \rangle$ profiles, the $\langle v'^2 \rangle$ profiles show a similar trend in that the there is greater velocity shear near the walls with a larger shear near the rough wall as expected. Near the centerline, both profiles decrease in magnitude. The profiles differ in that the magnitudes of $\langle v'^2 \rangle$ are less than $\langle u'^2 \rangle$ due to v' being damped by the presence of the wall.

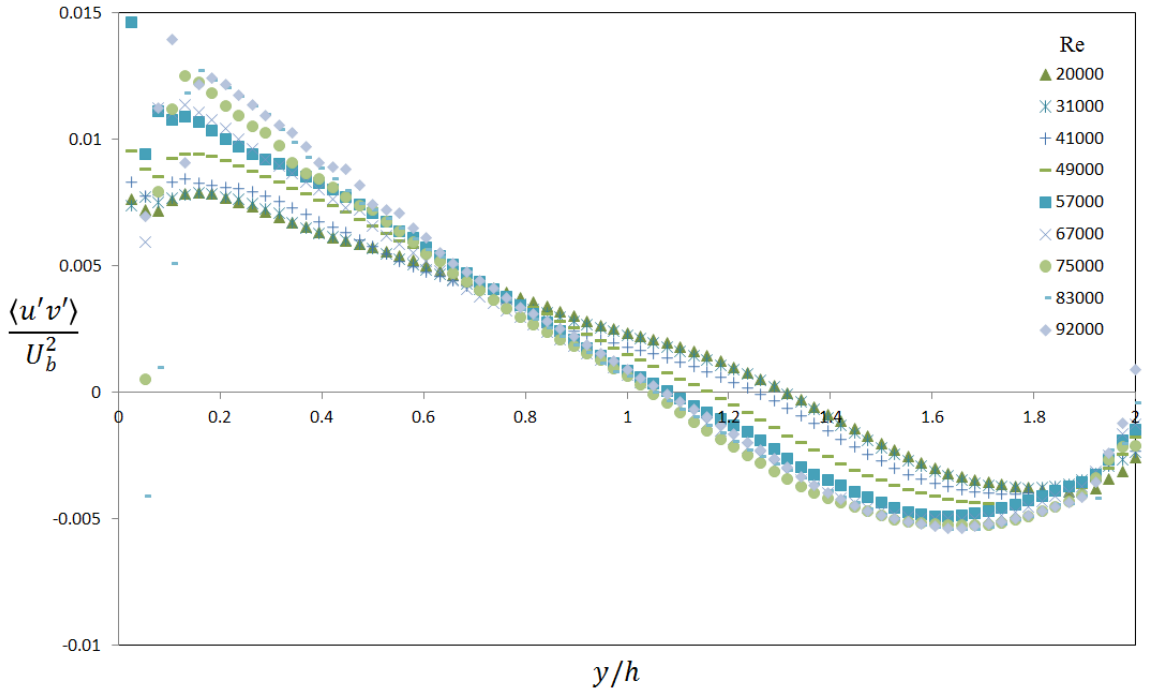

Figure 4.4: Full range of $\langle u'v' \rangle$ profiles for all non-blowing cases.

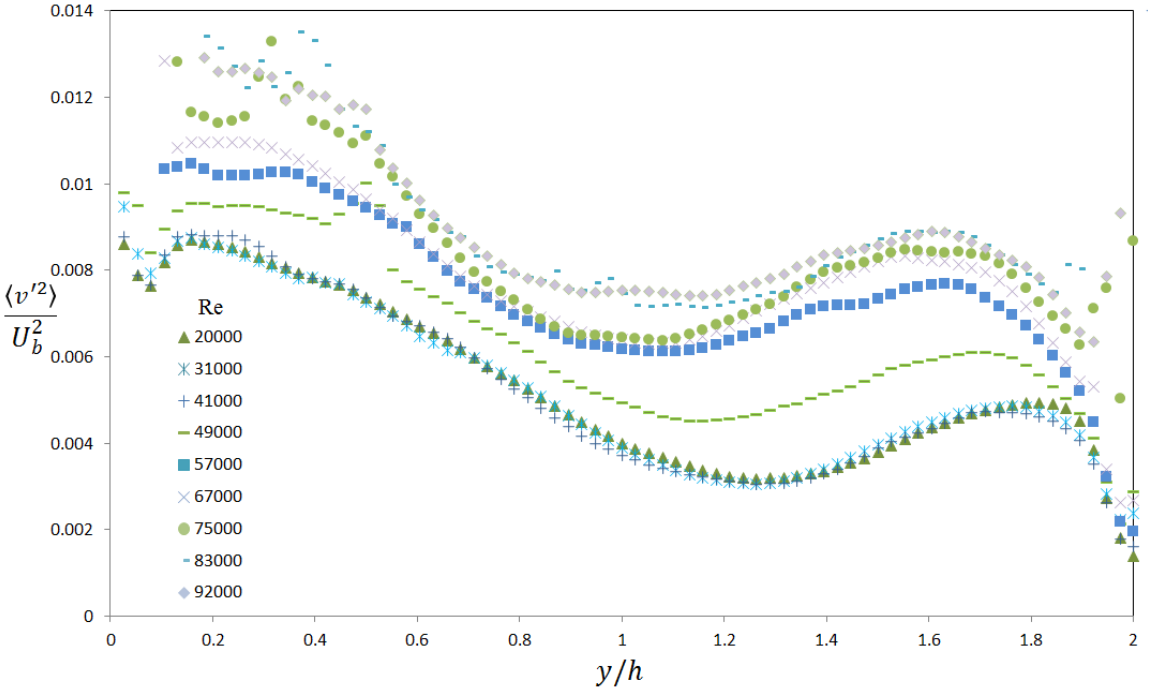

Figure 4.5: Full range of $\langle v'^2 \rangle$ profiles for all non-blowing cases.

4.1.2 Blowing Cases

The streamwise velocity profiles for each of the blowing cases and Reynolds numbers can be seen in fig. 4.6. For each Reynolds number, all of the blowing cases are plotted along with the non-blowing case. Overall, the addition of blowing acts to shift the profiles from a nearly symmetric profile without blowing, to an asymmetric one. The shift causes the maximum velocity to be located at around $1.6h$, which is near the smooth wall. The addition of blowing also decreases the velocity near the rough wall. This can be explained by the blowers suctioning the air and pulling it through the porous surface. With increasing Reynolds number, the difference between the blowing and non-blowing profiles becomes more apparent. Also, at the higher Reynolds numbers, the change in BR begins to have a decreasing effect on the mean flow. This effect is more apparent near the walls where the profiles nearly collapse as the BR changes.

The wall-normal velocity profiles for each of the blowing cases and Reynolds numbers can be seen in fig. 4.7. As with the non-blowing cases, the uncertainty in the PIV measurements was greater than the actual velocity in the channel. As expected, the profiles remain relatively constant across the height of the channel. The only exception occurs in the lowest Reynolds number blowing cases seen in fig. 4.7. For the .75% and .98% BR cases, the profiles appear to vary linearly with a slight negative velocity near the rough wall to a positive one near the smooth wall. In this frame of reference, the negative velocity indicates that the flow was moving in the direction of the rough wall. This does not make sense, since the injected flow would be moving away from the rough wall. This is a non-physical result, so this can be ignored. While the change in direction of the flow is significant in those cases, the overall magnitude was within $\pm$ 3% of U_b. For the .98% BR case at $Re = 20000$, the measured V_0, which was the injected flow velocity, was 0.0345 m/s. With a bulk velocity of 1.84 m/s for that case, this meant that near the rough wall a $\langle V \rangle / b$ of 0.019 would be expected.

Based on the plot, the velocity is around 0.023 that of U_b. This lends credit to the possibility that the PIV was unable to resolve the lower magnitudes of $\langle V \rangle$. The $Re = 92000$ case seen in fig. 4.7 is also worth mentioning due to the apparent scatter near the walls. This can be seen as the large sporadic magnitudes of $\frac{V}{U_b}$. This scatter was caused by the limitations of the PIV system in it's inability to capture particle pairs at the edges of the field of view.

The Reynolds normal stress profiles of $\langle u'^2 \rangle$ for all blowing cases is shown in fig. 4.8. The shape of the profiles differ greatly between the blowing and non-blowing cases. The addition of blowing nearly linearizes the profiles with the majority of the turbulence being generated near the rough wall. The exceptions are the $Re = 92000$ blowing cases where the profiles appear to have a similar shape but shifted compared to the non-blowing case. This can be attributed to the data scatter associated with the higher Re.

The Reynolds shear stress profiles of $\langle u'v' \rangle$ for all blowing cases is shown in fig. 4.9. It is apparent that addition of blowing acts to shift the slope of the profiles. This can be explained by the addition of the injected flow in which V now becomes significant in the channel. The increase of BR also appears to increase the magnitude of $\langle u'v' \rangle$. This effect diminishes at higher tunnel speeds which can be seen by the blowing profiles collapsing.

Significant change in the shape of the blowing and non-blowing profiles of the Reynolds stress $\langle v'^2 \rangle$ component can be seen in fig. 4.10. For the no-blowing cases, the profiles are bimodal and associated with turbulence generation at each wall. However, with the addition of blowing, the profiles begin to take a more linear shape with increasing BR and Re.

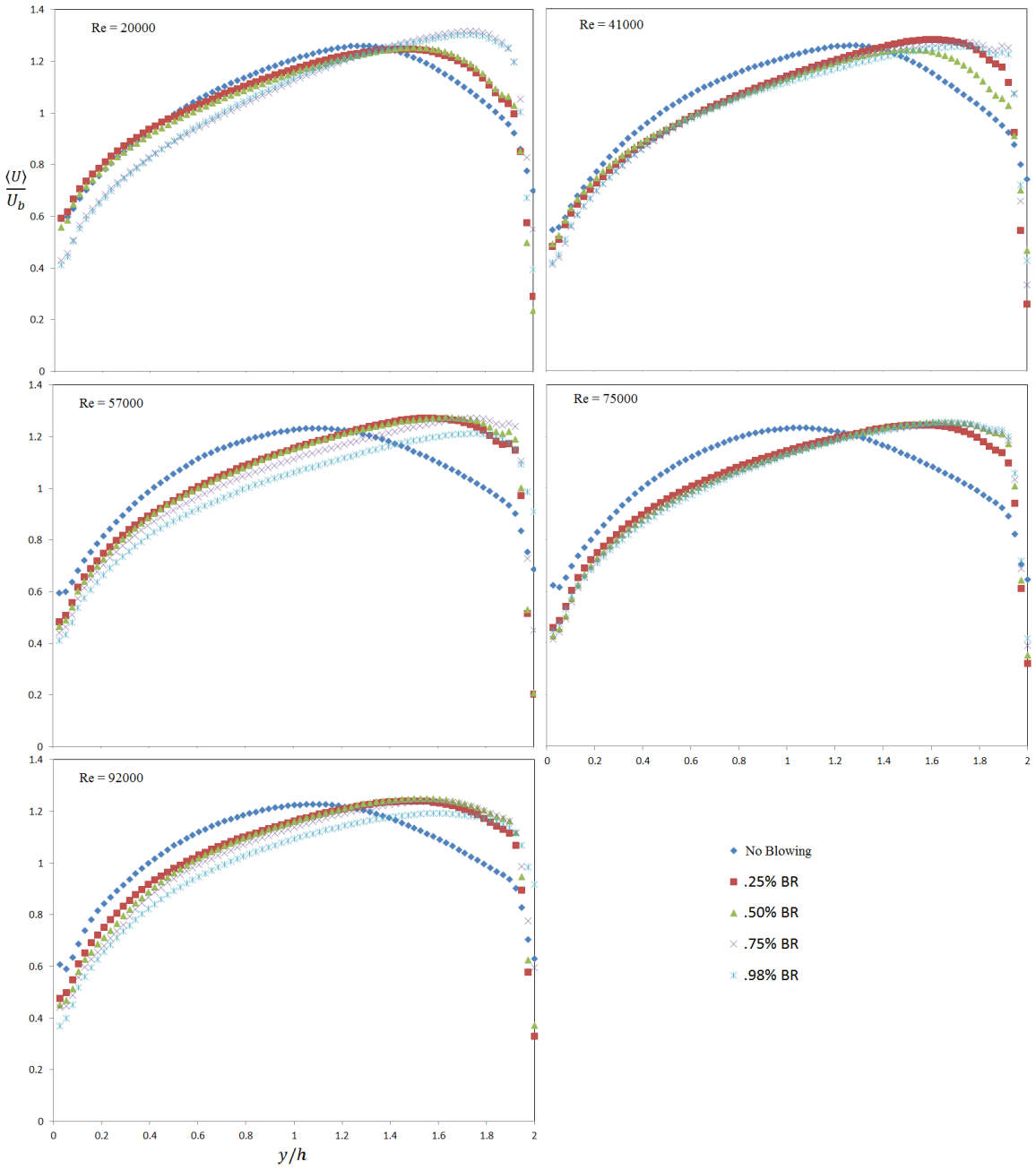

Figure 4.6: Streamwise velocity profiles for all blowing cases. Symbols for each BR shown in the plot.

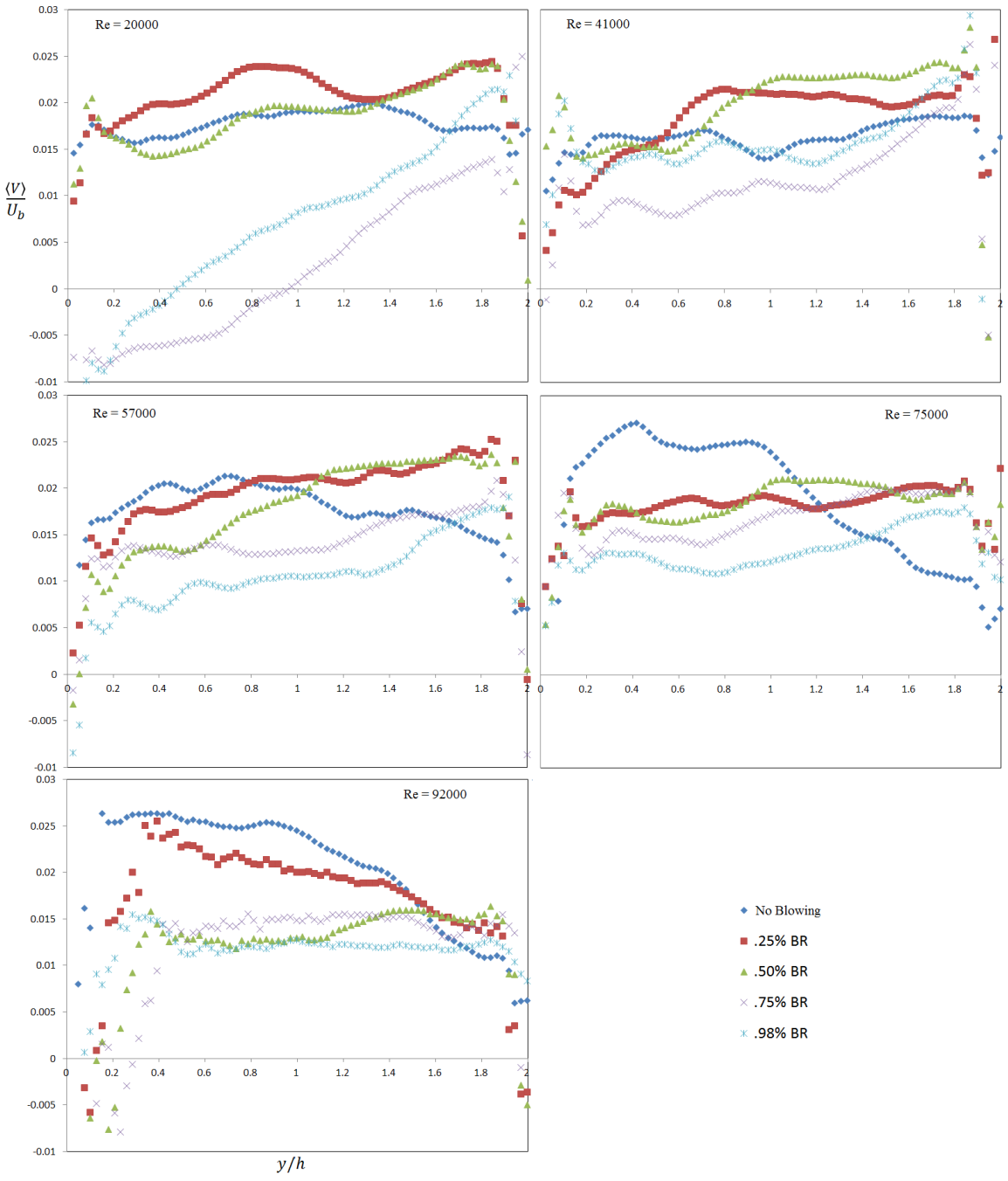

Figure 4.7: Wall-normal velocity profiles for all blowing cases. Symbols for each BR shown in the plot.

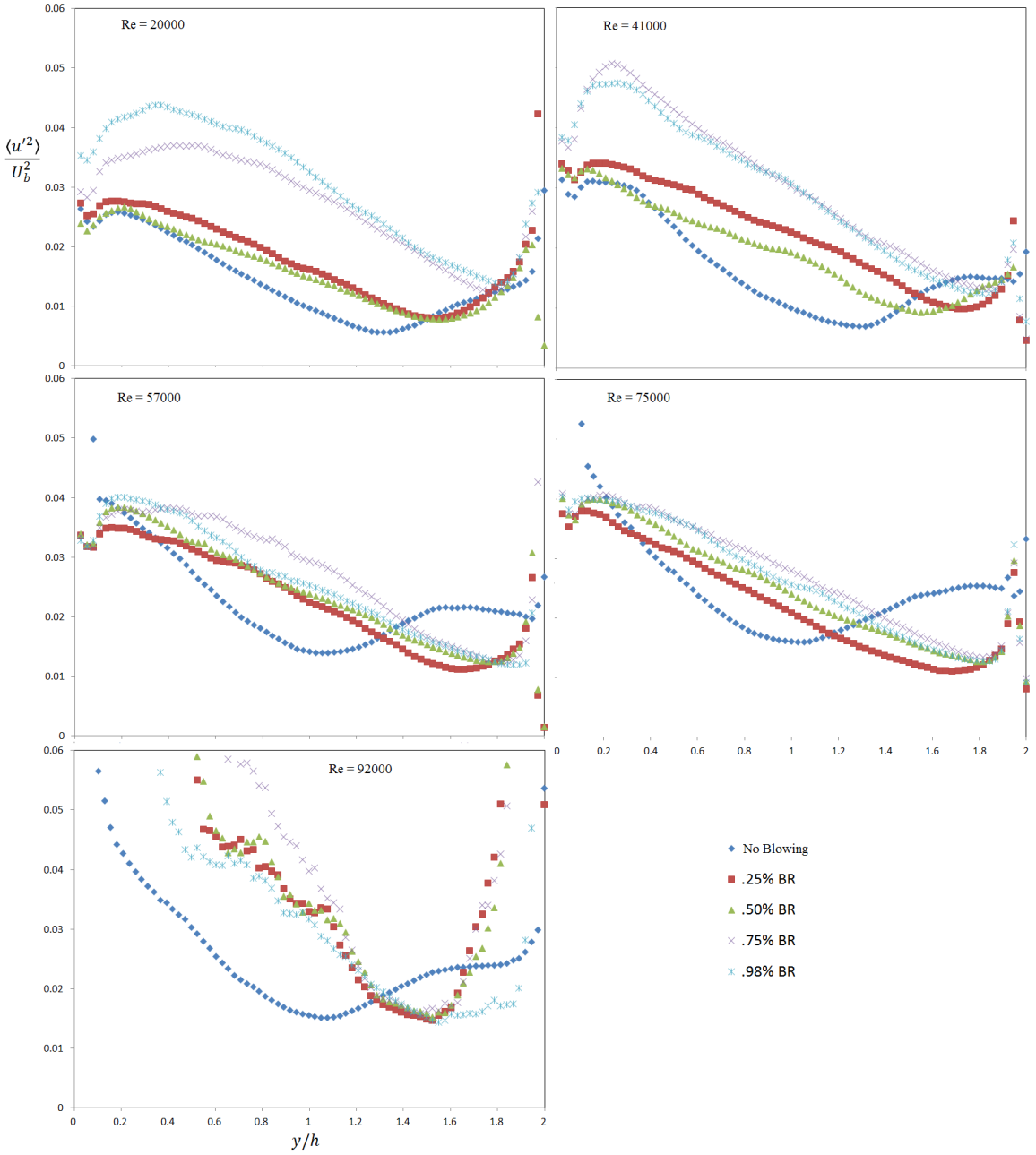

Figure 4.8: Reynolds stress profiles of $\langle u'^2 \rangle$ for all blowing cases. Symbols for each BR shown in the plot.

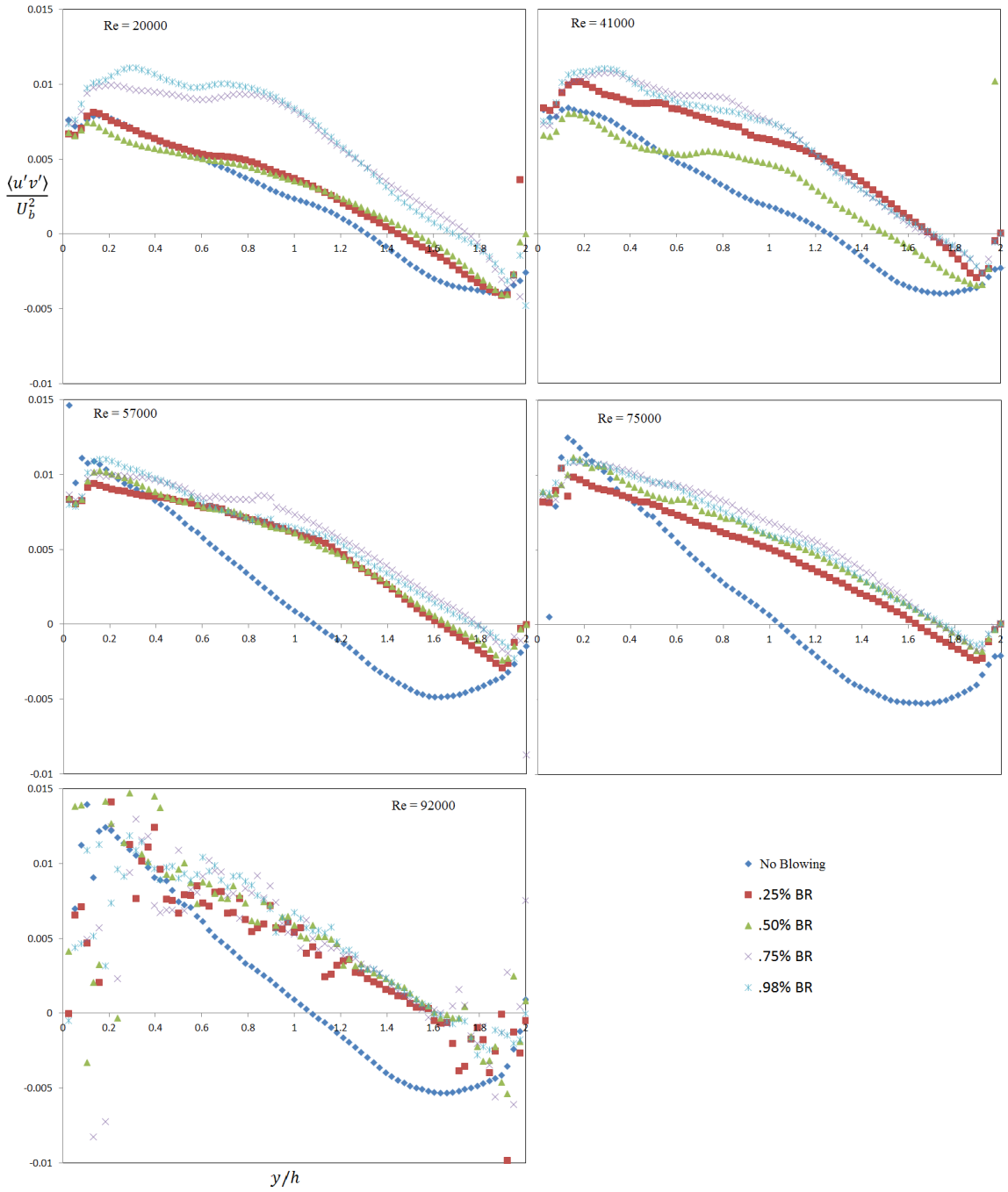

Figure 4.9: Reynolds stress profiles of $\langle u'v' \rangle$ for all blowing cases. Symbols for each BR shown in the plot.

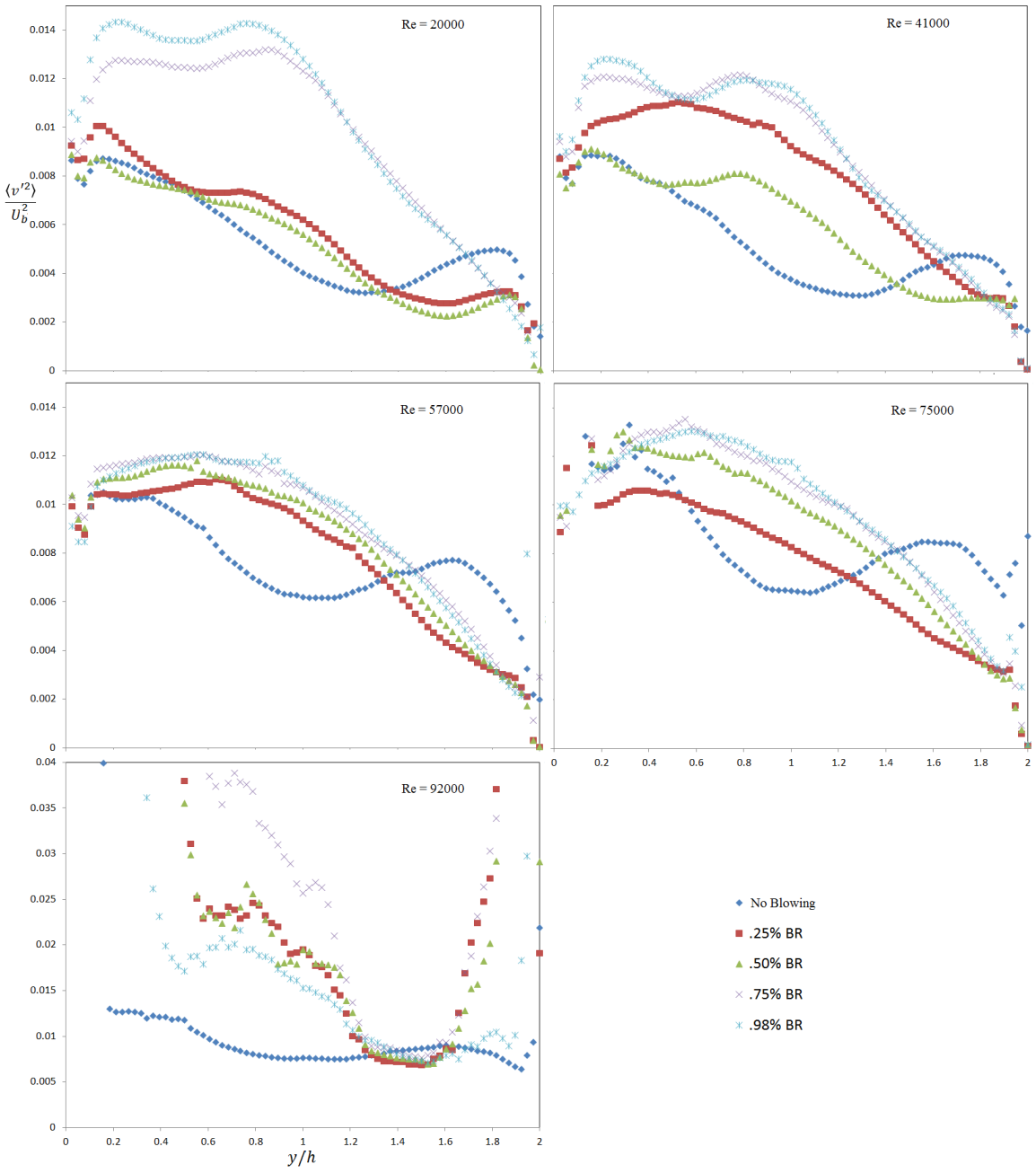

Figure 4.10: Reynolds stress profiles of $\langle v'^2 \rangle$ for all blowing cases. Symbols for each BR shown in the plot.

4.2 Shear Stress Profiles

Referring back to eq. 2.42 in section 2.8, the determination of τ required the measurement of $\partial\langle U\rangle/\partial y$, $\langle u'v'\rangle$, $\langle U\rangle$, and V_0. These were then used to calculate τ at each point in the profile. A line could then be fit to each of the profiles and extrapolated to the rough wall in order to determine τ_w. This line was fit near the centerline where the data was relatively scatter free ($0.6 < y/h < 1.4$). Again, this section is split up with the non-blowing cases shown first followed by the blowing cases. In each of the profiles, τ_w is represented by c_f which depends upon τ_w.

4.2.1 Non-Blowing Cases

The full range of shear stress profiles for all non-blowing cases are shown in fig. 4.11 and 4.12. In each of the cases the location in the channel where $c_\tau = \tau/(0.5\rho U_b^2) = 0$ corresponding to $\tau = 0$ occurs at around .06 m from the rough wall, or about .01 m from the centerline towards the smooth wall. In channel flow with smooth walls, this zero crossing would be located at the centerline with equal values of $c_\tau = c_f = \tau_w/(0.5\rho U_b^2)$ at the walls. The profile behavior is linear as expected near the centerline however the linearity disappears near the walls. As noted previously, according theory, the profiles should remain linear across the entire channel. These differences in behavior are attributed to the inaccuracy of the PIV near the walls introduced by reflection of the light sheet and high velocity gradients causing inaccurate averaging within the interrogation volume. Also, the smooth wall conditions might not have been fully developed since the suction will stabilize the turbulence and slow down the mixing. It is also worth noting that the rough wall caused an increase in magnitude of c_τ with the increase in c_f appearing as a shift in the profile towards the smooth wall. The increasing Reynolds number also causes an increase in magnitude of c_τ which is also expected due to the increased magnitude of the Reynolds shear

stress.

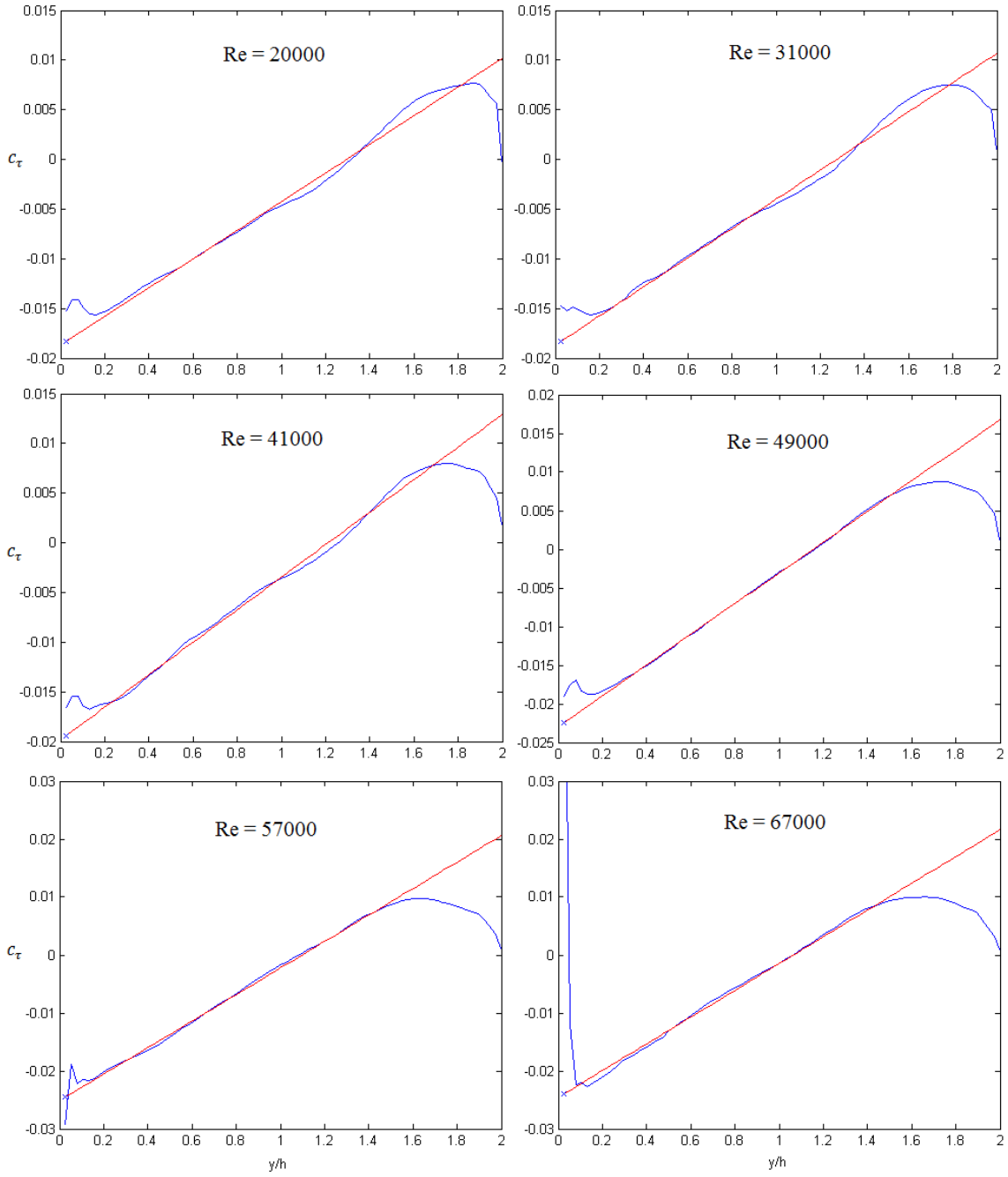

Figure 4.11: c_τ profiles. Associated Reynolds numbers shown in each profile. Red line shows determined fit used to find τ_w.

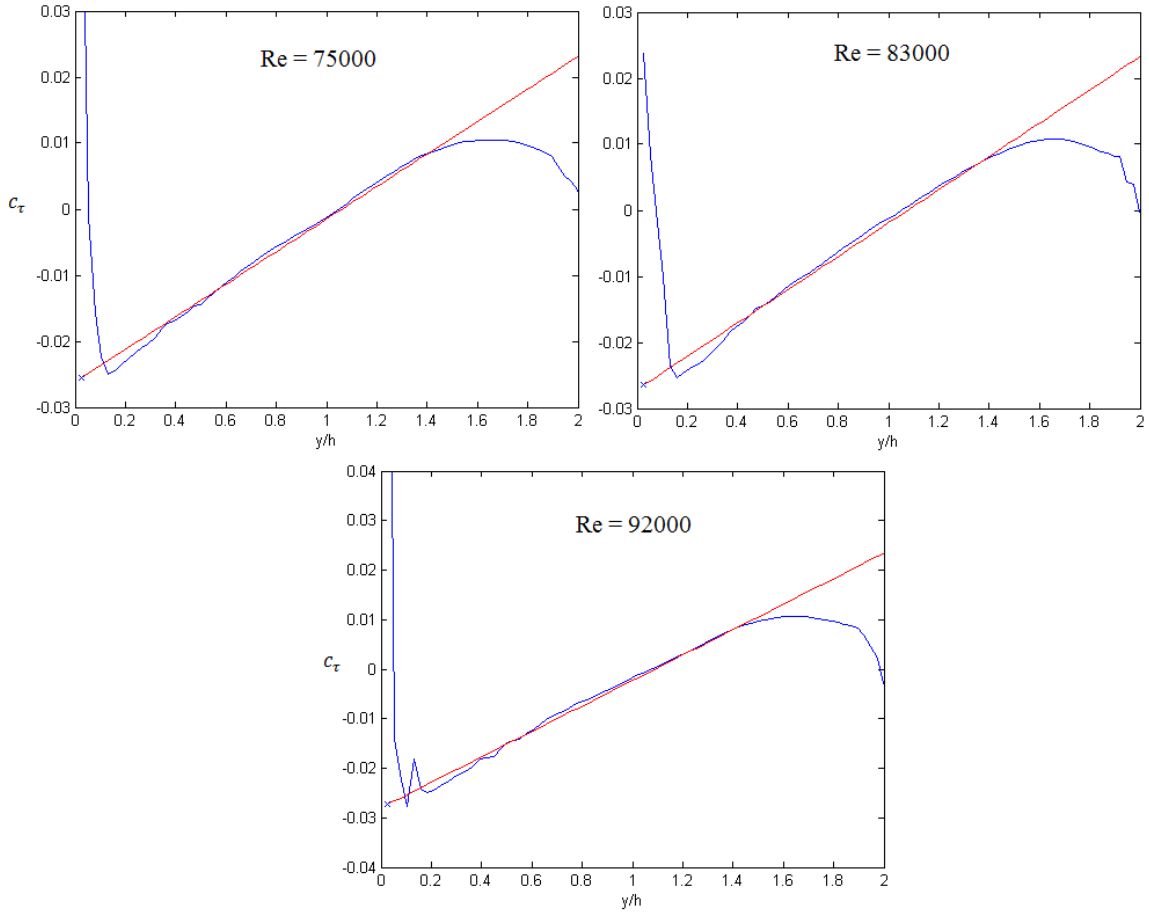

Figure 4.12: c_τ profiles. Associated Reynolds number shown in each profile. Red line shows determined fit used to find τ_w.

4.2.2 Blowing Cases

The full range of shear stress profiles for all blowing cases are shown in fig. 4.13 - 4.17. Each figure contains all BR cases at the specified Re. It is apparent that the addition of blowing acts to decrease c_f and shift the zero crossing of the c_τ profiles towards the rough wall. This effect increases with increasing BR. This behavior is comparable with that of Voisinet [5] which also showed a decrease in τ_w and consequently, c_f with increasing flow injection.

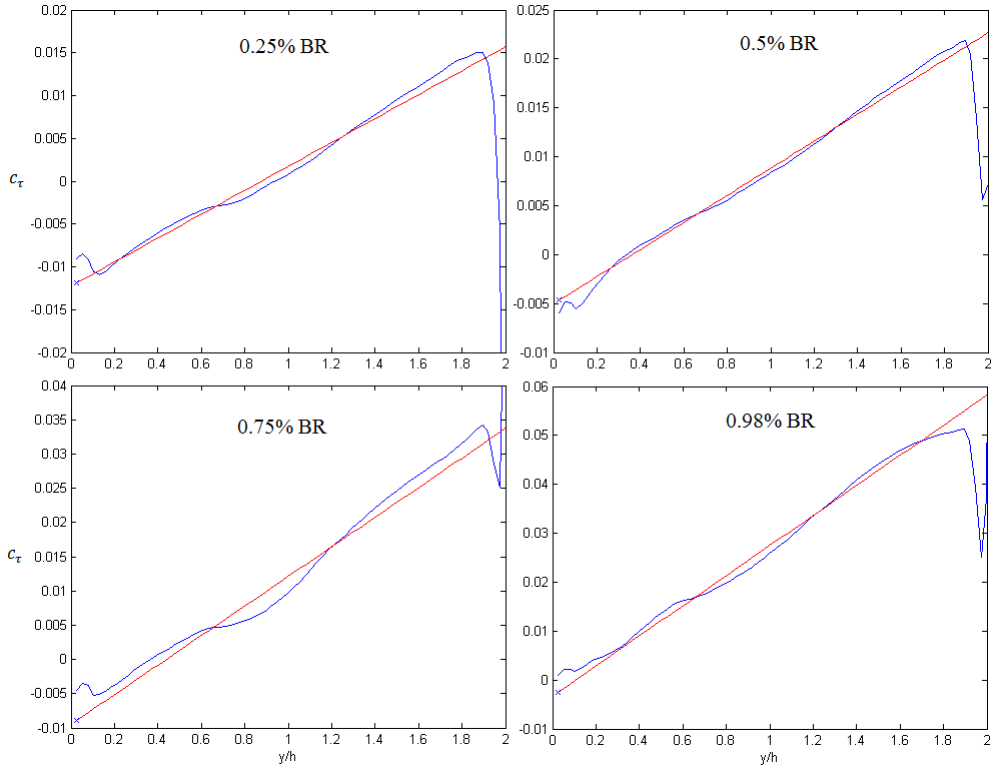

Figure 4.13: c_τ profiles at $Re = 20000$ for all blowing cases. Red line shows determined fit used to find τ_w.

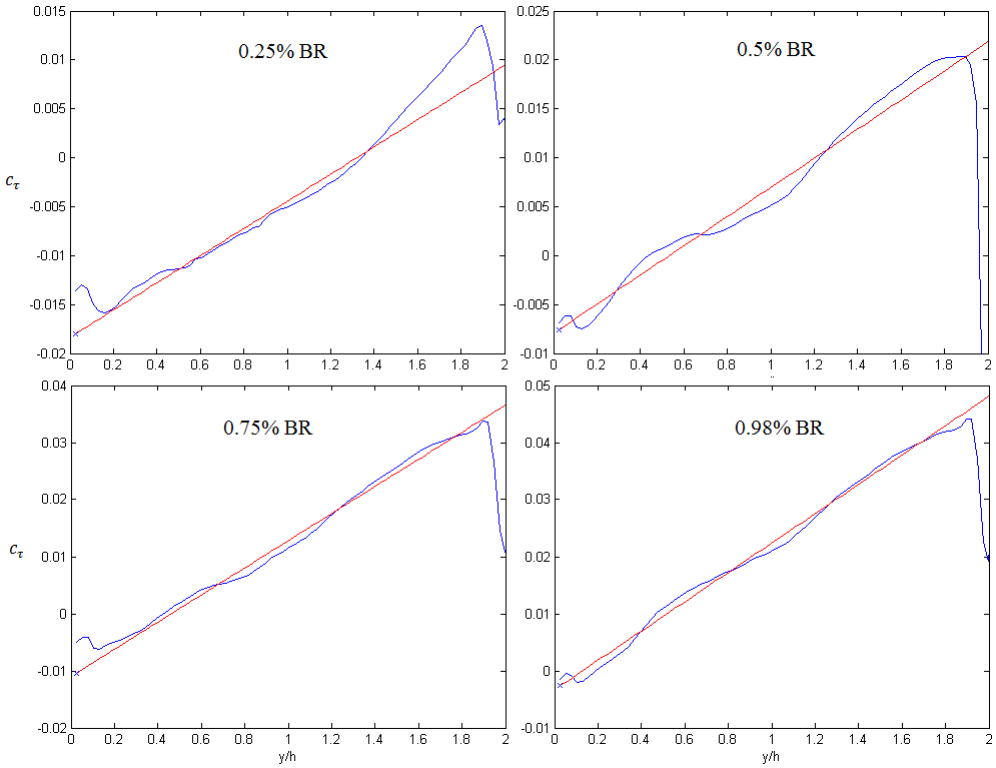

Figure 4.14: c_τ profiles at $Re = 41000$ for all blowing cases. Red line shows determined fit used to find τ_w.

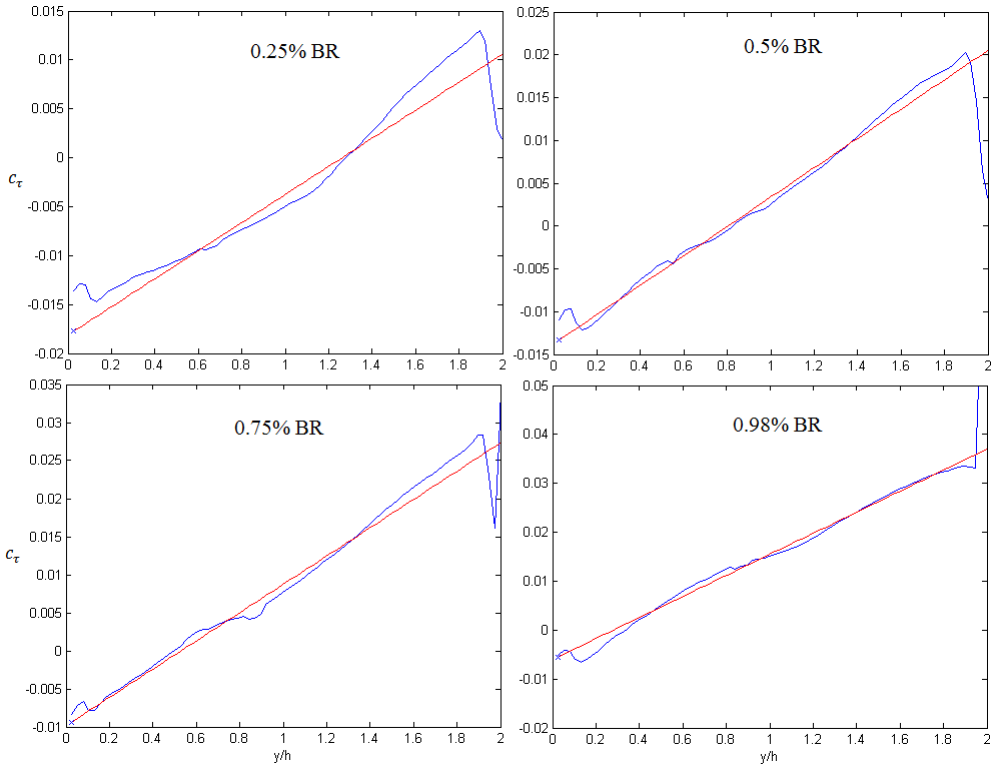

Figure 4.15: c_τ profiles at $Re = 57000$ for all blowing cases. Red line shows determined fit used to find τ_w.

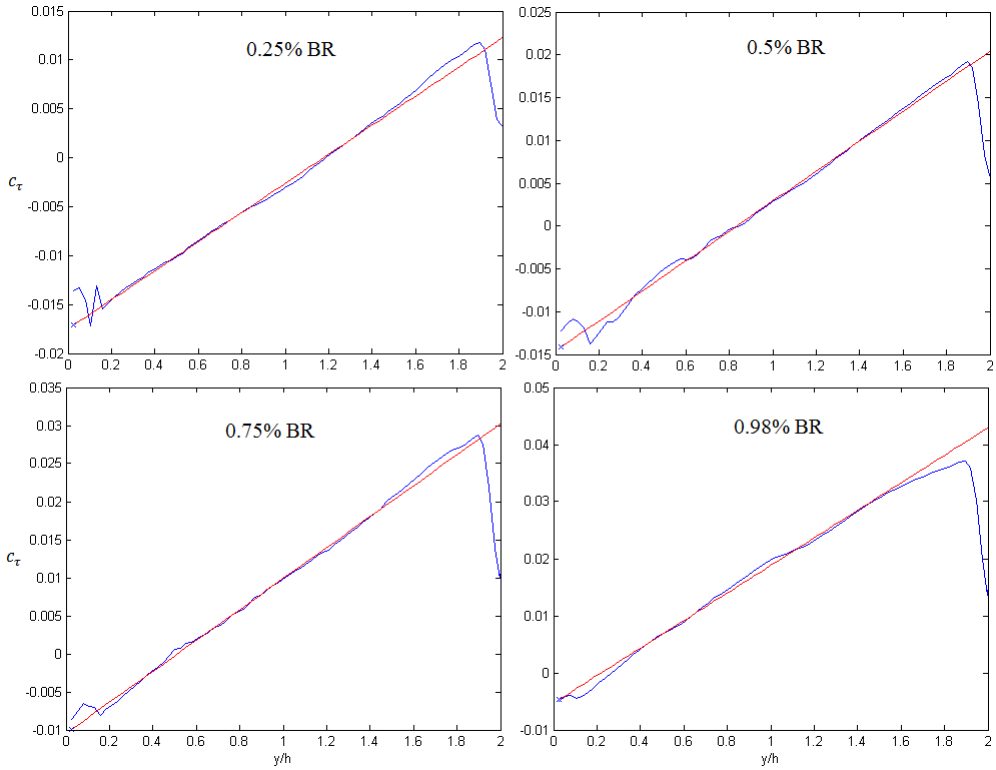

Figure 4.16: c_τ profiles at $Re = 75000$ for all blowing cases. Red line shows determined fit used to find τ_w.

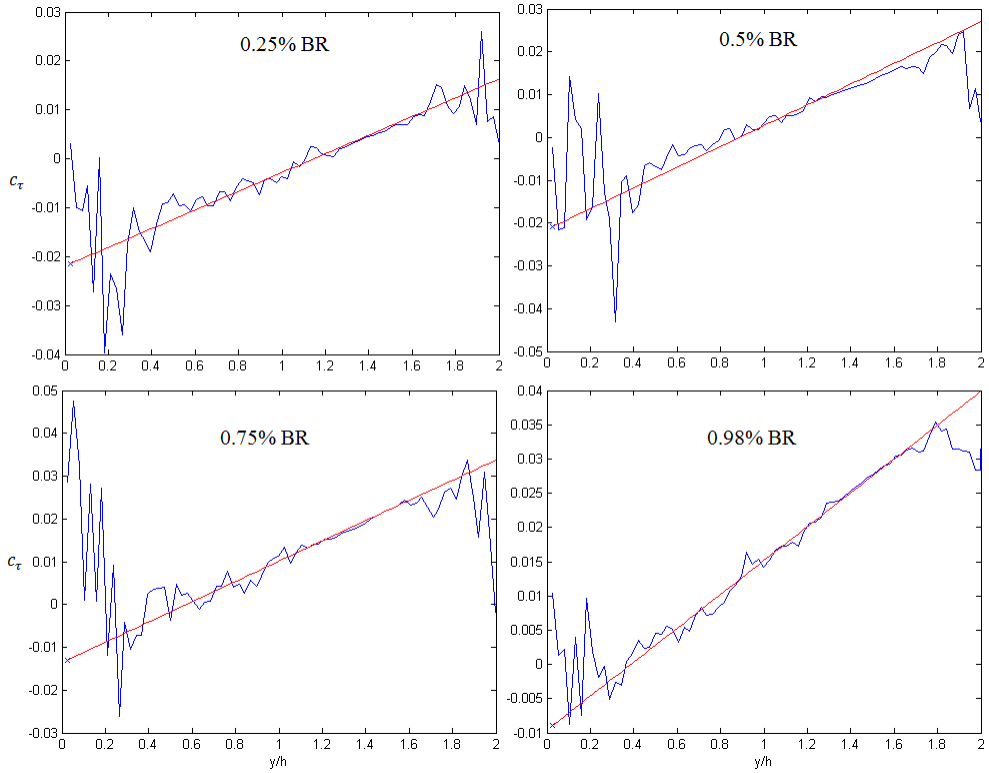

Figure 4.17: c_τ profiles at $Re = 92000$ for all blowing cases. Red line shows determined fit used to find τ_w.

The overall shear stress, τ at any given point in the profile is composed from three different contributions in the presence of blowing. These contributions can be seen in each term of eq. 2.42 in section 2.8. The first term is known as the viscous shear stress represented by

$$\rho\nu\frac{\partial\langle U\rangle}{\partial y}. \tag{4.3}$$

The next term is known as the Reynolds shear stress given by

$$-\rho\langle u'v'\rangle. \tag{4.4}$$

Finally, the last term is the shear stress due to blowing given by

$$-\rho V_0\langle U\rangle. \tag{4.5}$$

Each of these stresses contribute by varying degrees to τ, depending on y. To investigate the individual contributions to τ, profiles of each contribution was plotted alongside τ in fig. 4.18 and 4.19.

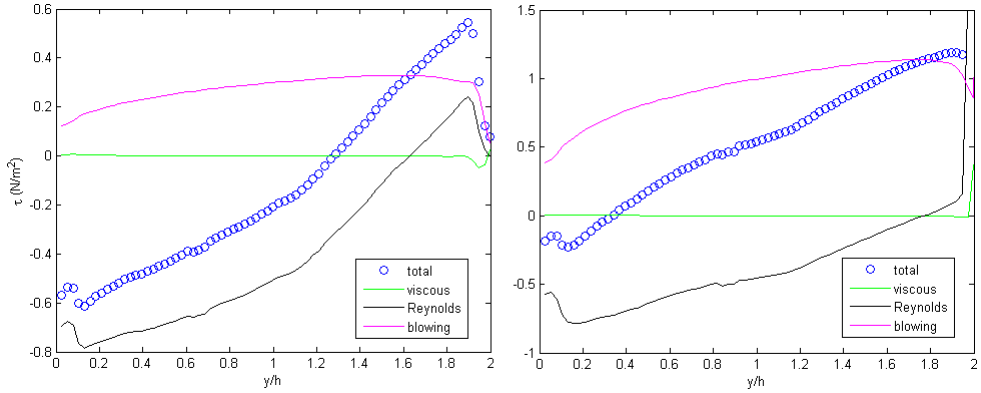

Figure 4.18: Shear stress contributions for $Re = 57000$. $BR = 0.25\%$ (left), $BR = 0.98\%$ (right)

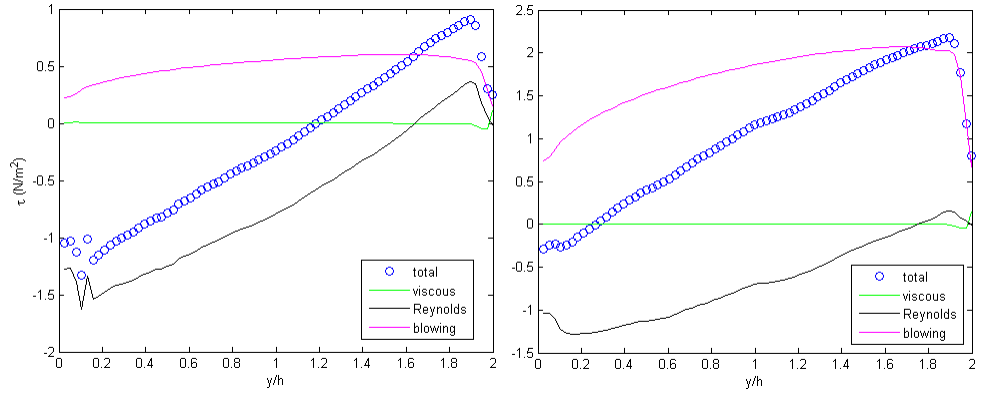

Figure 4.19: Shear stress contributions for $Re = 75000$. $BR = 0.25\%$ (left), $BR = 0.98\%$ (right)

Due to the inability to measure near the walls where the viscous stresses dominate, the viscous stresses measured in this experiment remain a relatively insignificant contribution to the overall shear stress. This meant that the analysis to determine τ_w weighed heavily on the interactions between the Reynolds stress and blowing shear stress contributions. Looking at the lower BR for each Reynolds number shown, the Reynolds stress follows closely in shape and magnitude to the overall shear stress.

The addition of blowing appears to shift the overall shear stress vertically to a degree depending on the BR. This shift increases with increasing BR.

4.3 Wall Shear Stress Modification

It was also of interest and the primary objective of this thesis to quantify the effect of blowing on the measurement of τ_w. These effects are shown in fig. 4.20 in which the ratio of τ_w with blowing to τ_w without blowing are shown as a function of the $\%BR$. The Reynolds numbers shown in 4.20 represent each of the 5 Reynolds numbers that were subjected to flow injection and were calculated using the bulk velocity U_b, and the height of the channel H. With increasing $\%BR$, the overall effect of blowing on τ_w appears as a linear decrease with the .98% BR cases having approximately 20% of the τ_w measured without blowing. Although difficult to discern due to scatter in the results, which can be seen by the large error at the highest Re, the decrease in wall shear stress due to increase in blowing rate also appears to be independent of Re.

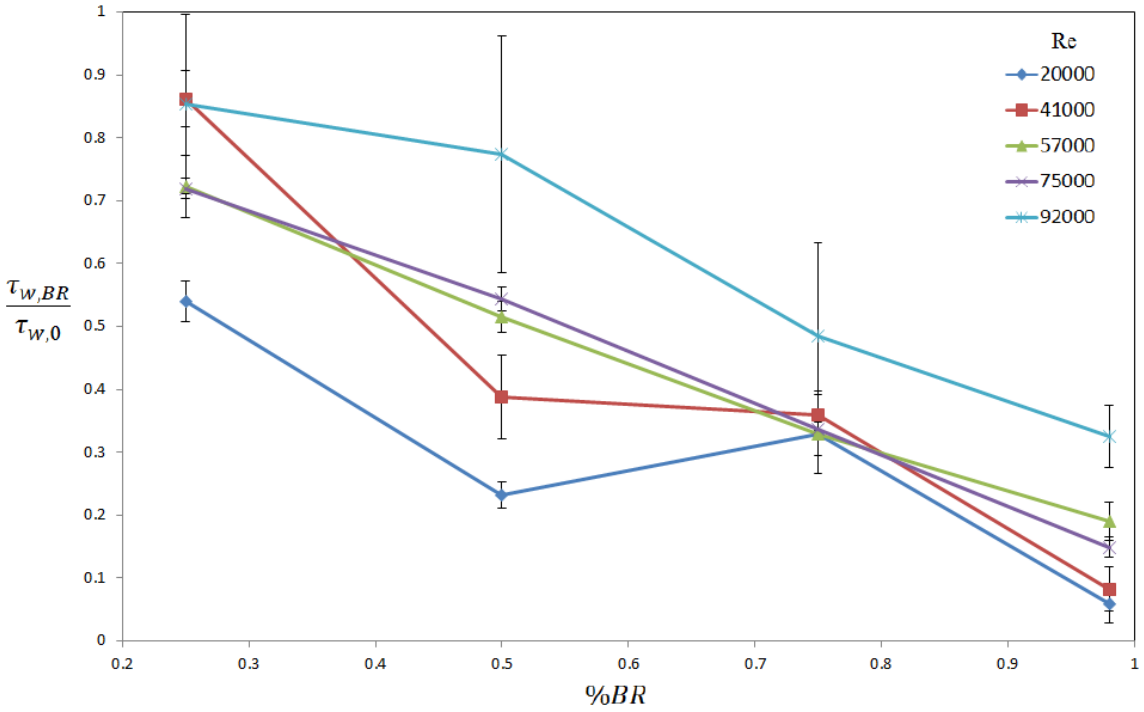

Figure 4.20: τ_w augmentation due to blowing.

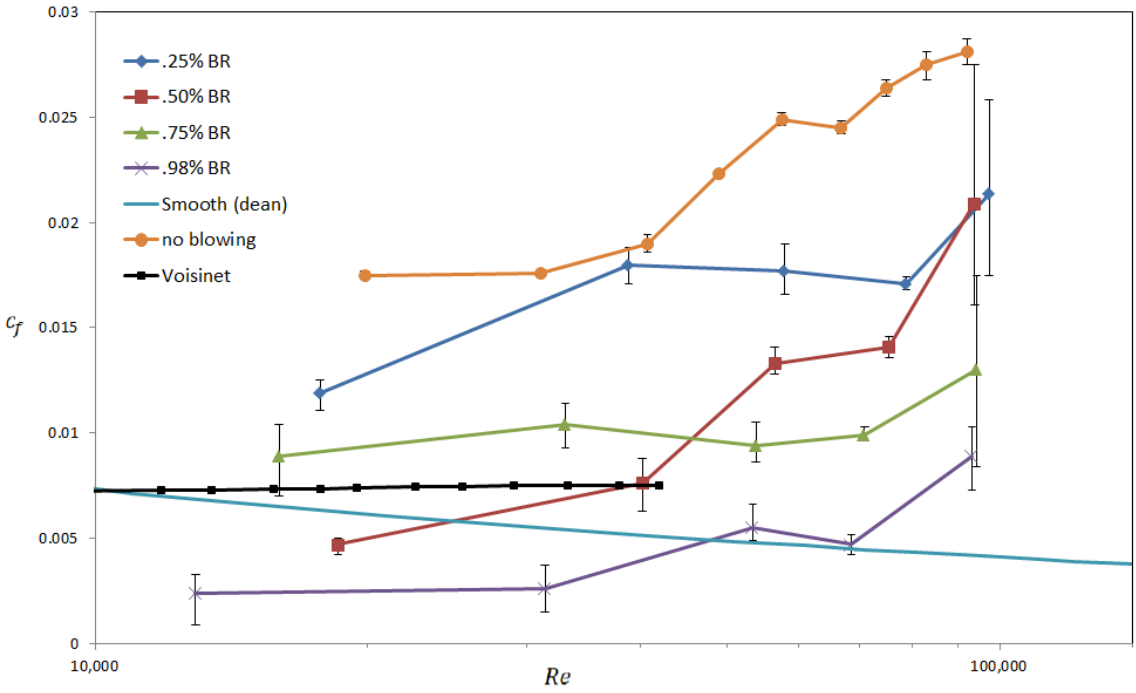

Figure 4.21: Skin friction coefficient as a function of Reynolds number.

The modification of τ_w and resulting c_f due to roughness and blowing can be compiled into a figure similar to the Moody diagram as shown in fig. 4.21. Here, the curves are compared to smooth wall data compiled from Dean [14] as well as rough wall data from Voisinet [5]. There is clear indication that the addition of blowing acts to reduce c_f with increasing BR. This effect allows c_f to be reduced to below smooth wall results for the higher BR cases. Overall, the curves remain fairly constant indicating the flow has reached fully rough conditions with little change in c_f with increasing Reynolds number. However, there is a slight increase in c_f for the higher Reynolds number cases. While this may hint at the flow still being transitional, it was concluded that this increase could be attributed to uncertainty and data scatter which was more apparent in the higher Re cases as shown by the error bars.

The inner-scaled mean velocity plots, using the τ_w determined above, are shown in fig. 4.22. It is apparent that the increase Reynolds number causes an increase in ΔU^+. This is expected and corresponds to an increase in τ_w due to increasing k^+.

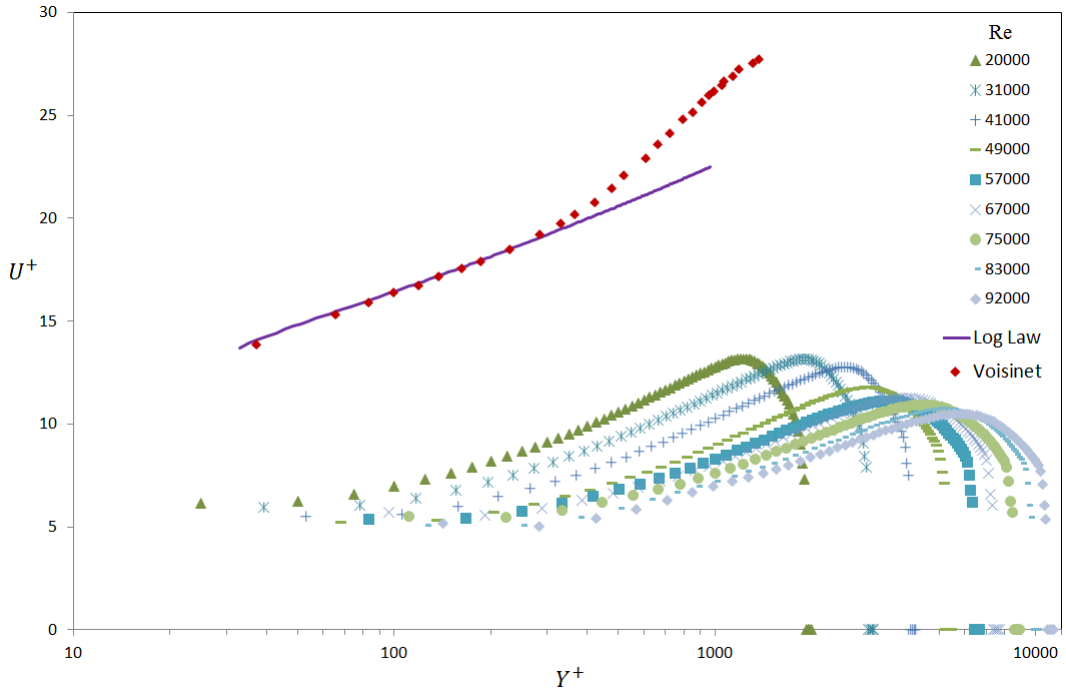

Figure 4.22: Inner-scaled mean velocity plots for all non-blowing cases. Rough wall data from Voisinet from Ref. [5].

These results are compared to those from Voisinet [5] in which the selected data set is of a rough surface with $k = 0.1$ mm at a $k^+ = 5.5$. The rough surface used in this experiment which was characterized in section 3.4 had an average $k_{rms} = 0.36$ mm with k^+ ranging from 6.6 for the $Re = 20000$ case to 38.6 for the $Re = 92000$ case. The larger ΔU^+ in the TPS analog surface plots compared to Voisinet's surface is also expected in that the roughness had a greater influence on the mean flow near the wall due to the larger roughness elements.

The inner-scaled mean velocity plots for each of the blowing cases is shown in figure 4.23. These were plotted alongside the theoretical log-law for the smooth wall case for comparison ($\kappa = 0.4, B = 5.5$). Voisnet's work [5] examined a rough surface which was subjected to mass flow rates up to 0.146 $\frac{kg}{m^2 sec}$. In Voisinet's results, the addition of blowing acted to increase the roughness effects and cause an additional downward shift in U^+. These results were also seen in Miller [3]. The results in this work show different behavior, with the addition of blowing causing an upward shift. This shift

becomes less apparent with increasing tunnel speed.

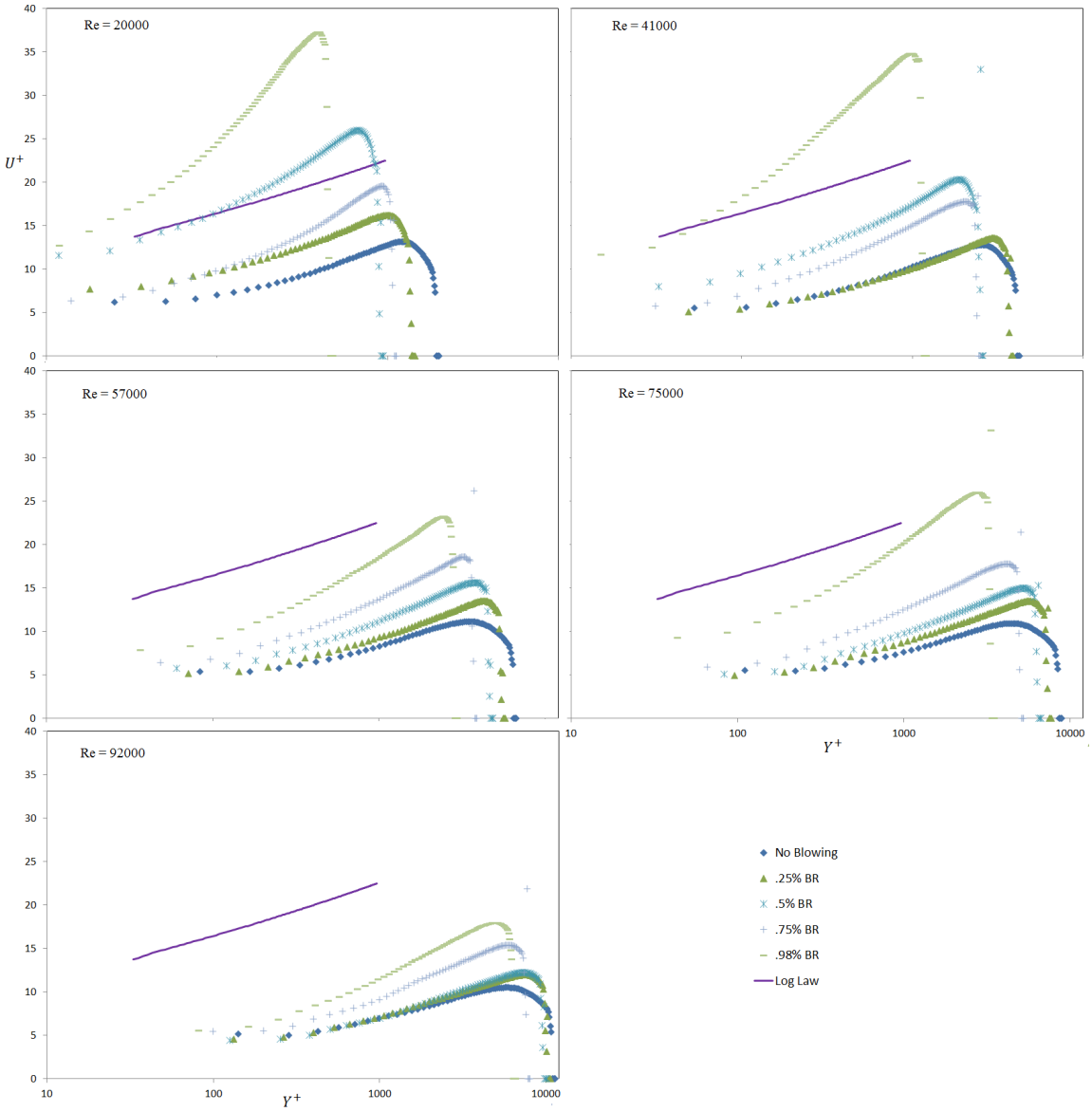

Figure 4.23: Inner-scaled mean velocity profiles for all blowing cases. Rough wall data from Voisinet from Ref. [5]

.

4.4 Measurement Comparison to Clauser Method

Due to the unique approach in the measurement of τ_w in this thesis, there needed to be some sort of basis of comparison of the results with some other known method. The "Clauser chart" method has been used before in rough-walled turbulent boundary layers [60–62]. However, this method has been shown to lack agreement with other methods [63]. The basis of the Clauser method's reliability is the assumption that the velocity-defect law exists for a given wall-bounded flow. It involves utilizing the streamwise Reynolds stress, $\langle u^{2'} \rangle$ to find the correct zero-plane displacement, y_o, as discussed in eq. 2.14 in chapter 2. The slope of the inner-scaled mean velocity profile is then modified by changing U_τ to match the slope of the smooth-walled case in order to find the corrected U_τ.

For each Re and BR tested, the Clauser method was applied to estimate U_τ. The Clauser fit and RANS-estimated U_τ values are shown in table 4.1 with the associated flow conditions for each case shown in table 3.1. There is good agreement between the two U_τ values for the non-blowing cases. The values begin to diverge however as BR is increased. This warranted further investigation into the potential causes of the divergence.

A potential cause of these differences was the significant modification of the wake region due to blowing and suction effects. Alternatively, the most likely source of error in the RANS-based method was error in the determination of V_0. To investigate this possibility, case numbers 8-11 were examined in more detail in which V_0 was artificially adjusted until U_τ matched the Clauser method result. This produced percent differences of 29.84% between the RANS estimated and adjusted Clauser method values of V_0 for the $BR = 0.25\%$ case which increased up to 112.53% for the $BR = 0.98\%$ case. It was then necessary to determine which of the values could be trusted. This was accomplished by examining the shear stress profiles for the

measured and Clauser method values. A side-by-side comparison of the two profiles are shown in fig. 4.24. The difference in shape of the profiles is clear between the two cases. The Clauser method profile loses more linearity in τ which disagrees with theoretical expectations relative to the measured profile. This result indicates that the Clauser method loses validity with the addition of blowing and suction effects.

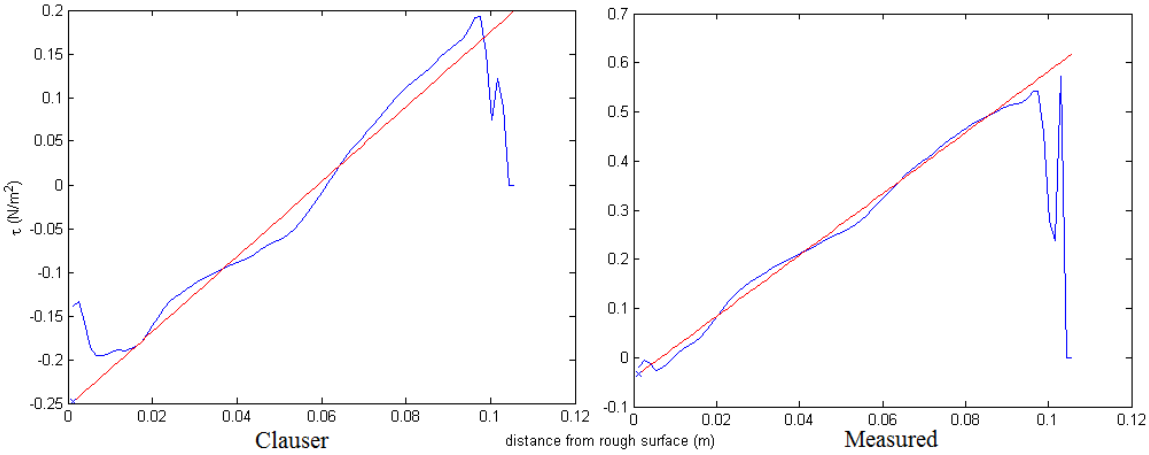

Figure 4.24: Shear stress profiles for Clauser method and measured results for 0.98% BR case.

Table 4.1: Clauser Method Comparison

Case	Re	BR %	u_τ (RANS)	u_τ (Clauser)
1	20000	0	0.265	0.28
2	20000	0.25	0.195	0.21
3	20000	0.5	0.128	0.22
4	20000	0.75	0.152	0.23
5	20000	0.98	0.065	0.205
6	31000	0	0.423	0.43
7	41000	0	0.573	0.57
8	41000	0.25	0.526	0.5
9	41000	0.5	0.353	0.47
10	41000	0.75	0.340	0.5
11	41000	0.98	0.163	0.45
12	49000	0	0.739	0.75
13	57000	0	0.907	0.9
14	57000	0.25	0.777	0.75
15	57000	0.5	0.657	0.7
16	57000	0.75	0.525	0.69
17	57000	0.98	0.399	0.85
18	67000	0	1.042	1.08
19	75000	0	1.206	1.2
20	75000	0.25	1.041	1.03
21	75000	0.5	0.905	0.96
22	75000	0.75	0.711	0.8
23	75000	0.98	0.473	0.85
24	83000	0	1.362	1.39
25	92000	0	1.535	1.58
26	92000	0.25	1.438	1.38
27	92000	0.5	1.369	1.35
28	92000	0.75	1.083	1.5
29	92000	0.98	0.887	1.4

Chapter 5 Conclusions

A turbulent channel flow wind tunnel was modified by addition of an apparatus to introduce mass injection through a rough surface combined with surface suction off the opposing surface. The apparatus was carefully designed to produce fully-developed turbulent channel flow with mass flux through the side walls. This apparatus was employed to characterize a surface roughness which was intended as an analog to a thermal protection system surface. The surface was characterized through the examination of wall shear stress, τ_ω, while being subjected to blowing and suction effects. An approach based on the idealized Reynolds Averaged Navier-Stokes (RANS) equations was used to determine τ_ω through the use of particle image velocimetry and knowledge of channel flow geometry. Time-averaged statistics were captured to gain insight into the effects due to blowing on the mean flow and Reynolds stresses. Through analysis of these statistics along with the modification to τ_ω, several conclusions can be drawn.

First, the rough surface used in this work acted to shift the zero crossing of the shear stress profiles towards the smooth wall. This was caused by the roughness elements introducing additional shear through τ_ω near the well relative to smooth wall flows. This is supported by the increase in Reynolds stresses near the rough wall compared to the smooth wall. There was also a clear shift in the profiles of the mean flow and Reynolds stresses between the blowing and non-blowing cases. The flow appeared to reach fully rough conditions. This is supported by the constant values for c_f with increasing Reynolds number.

Second, the addition of blowing acted to reduce τ_ω and consequently, c_f. This is supported by the shift in the zero crossing of the shear stress profiles towards the rough wall. This reduction is consistent with results seen in previous studies [5]. There is a decreasing effect due to blowing on the modification of τ_ω at higher tunnel speeds. This is supported by the decreasing ratio of τ_ω with blowing to τ_ω without blowing. This was also seen in the collapse of profiles of the varying BR for the mean velocities and Reynolds stresses.

The Clauser method to determine τ_ω was also found to lose validity in the case of flow injection and suction due to the significant modification of the wake region. This is supported with a comparison between the measured and Clauser fit values of U_τ. Looking at the shear stress profiles, the measured profiles followed expected linear behavior closer than the Clauser fit profiles.

Overall, the work in this thesis provided several original contributions. First, significant modifications to the channel flow facility had to be made to allow for fully developed turbulent flow with roughness, flow injection and suction effects. Next, the use of the RANS equations allowed for a novel approach to experimentally measure τ_ω. These measurements produced the first data set of turbulent channel flow with roughness, flow injection and suction effects.

These results will require further computational investigations in order to be validated. Future experimental work will need to be focused on improving the measurement of flow injection in order gain more insight in these effects on τ_ω. The unique rough surface used in this work will also allow for future comparisons to be made with actual ablative thermal protection system materials.

5.1 Appendix A: Uncertainty Analysis

Additional uncertainty analysis was needed in order to gain a sense of how accurate the measurements of τ_ω were. Referring back to eq. 2.42 in section 2.8, the shear stress at any given point was determined through measurement of the average streamwise velocity $\langle U \rangle$, and the average Reynolds stress $\langle u'v' \rangle$ component. As previously mentioned, these statistics were measured using PIV at the test section of the channel. The PIV images consisted of a grid of 50 by 80 individual values for each of the needed statistics. These values were then averaged in each row as described in equation 4.1 in section 4.1. The uncertainty in the final averages used in the shear stress analysis would thus come from the number of samples used in the row average of the PIV images. To quantify the uncertainty, an investigation was conducted in which sample size in the average for each row was varied in order to determine if the averages converge. These sample sizes were also varied at three different wall-normal positions in the channel ($y = 6.7, 26.7, 53.5$ mm). These plots can be seen in fig. 5.1. It is evident that as the sample size increases, $\langle U \rangle$ tends to converge to a constant average value. This is case for each measurement distance except at $y = 26.7$ mm where the average still seems to be changing even at the maximum sample size of 47 which was used in the analysis. As with all of the cases, the difference in $\langle U \rangle$ between the largest and smallest sample sizes are on the order of 10^{-3} m/s, which is relatively insignificant. It is therefore safe to assume enough samples were used for the average statistics in the shear stress calculations.

Another source of error was in the method employed to determine τ_ω at the rough wall. As discussed in section 2.8 the shear stress profiles were linearly fit and extrapolated to the rough wall. This meant that there was an error associated with the coefficients of the fit line that calculated for each Re and BR case. Using error analysis tools in Matlab, the error in the coefficients was calculated. This allowed for

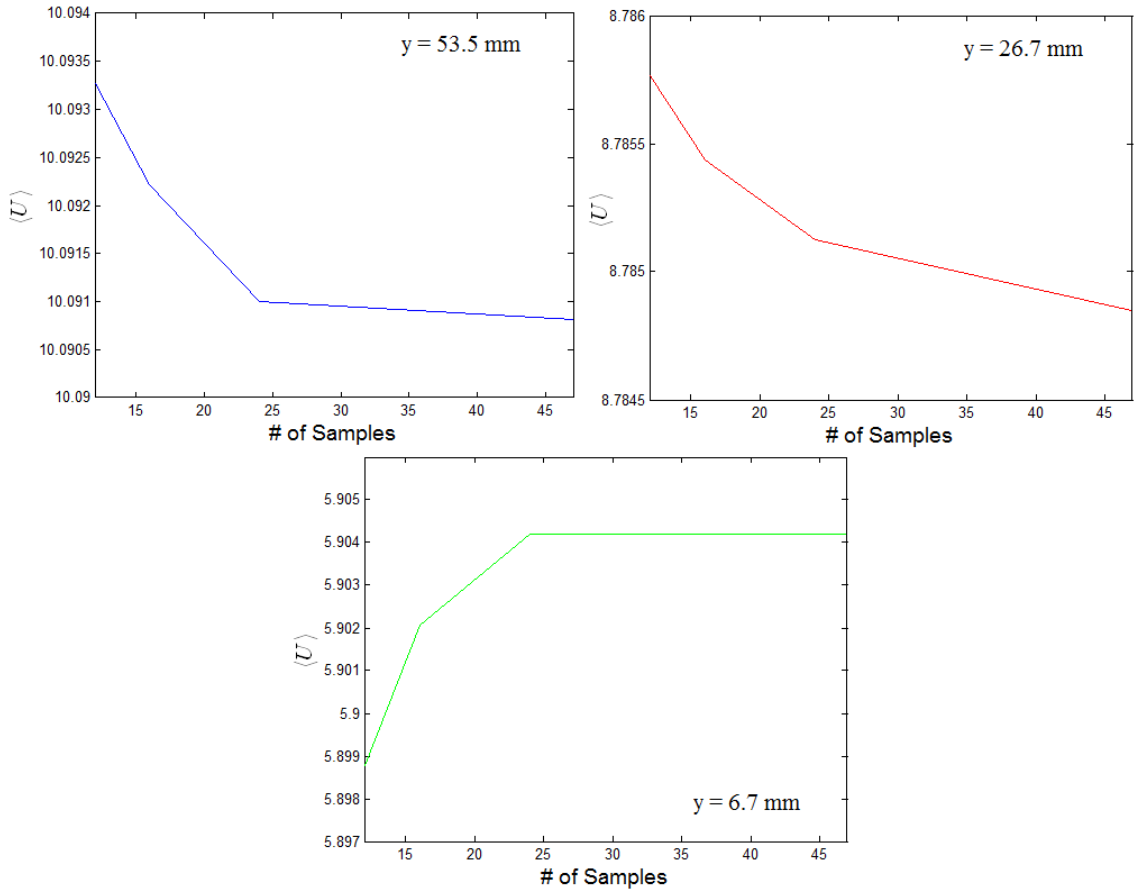

Figure 5.1: Convergence plots for each of the measurement distances. Distance shown in each plot.

an error estimate of τ_ω, which is denoted $\Delta\tau_\omega$. This error then had to be propagated to calculate c_f in which the associated errors for each measurement can be seen in figure 4.21 in section 4.3. This error was also propagated to determine the error in τ_ω augmentation due to blowing which is shown in fig. 4.20 also in section 4.3. A full list of the associated $\Delta\tau_\omega$ values for each case is shown in table 5.1.

Table 5.1: Errors in τ_ω based on coefficients of linear fit.

Case	Re	BR %	$\Delta\tau_\omega \left(\frac{N}{m^2}\right)$
1	20000	0	0.001
2	20000	0.25	0.003
3	20000	0.5	0.002
4	20000	0.75	0.005
5	20000	0.98	0.003
6	31000	0	0.003
7	41000	0	0.008
8	41000	0.25	0.016
9	41000	0.5	0.026
10	41000	0.75	0.015
11	41000	0.98	0.014
12	49000	0	0.003
13	57000	0	0.012
14	57000	0.25	0.050
15	57000	0.5	0.024
16	57000	0.75	0.035
17	57000	0.98	0.031
18	67000	0	0.018
19	75000	0	0.028
20	75000	0.25	0.022
21	75000	0.5	0.031
22	75000	0.75	0.021
23	75000	0.98	0.030
24	83000	0	0.054
25	92000	0	0.067
26	92000	0.25	0.417
27	92000	0.5	0.557
28	92000	0.75	0.442
29	92000	0.98	0.144

Bibliography

[1] S.B. Pope. *Turbulent Flows*. Cambridge University Press.

[2] H. Schlichting. *Boundary-Layer Theory*. New York: McGraw Hill.

[3] M.A. Miller. *Experimental Characterization of Roughness and Flow Injection Effects in a High Reynolds Number Turbulent Channel*. Dept. of Mech. Engrg., University of Kentucky.

[4] M.C. Wilder and D.C. Reda. Effects of distributed surface roughness on turbulent heat transfer augmentation measured in hypersonic free flight. *52nd AIAA Aerospace Sciences Meeting*, 2014.

[5] R. Voisinet. Influence of roughness and blowing on compressible turbulent boundary layer flow. *Technical report, Naval Surface Weapons Center, White Oak Lab, Silver Spring, MD*, June 1979.

[6] O. Reynolds. An experimental investigation of the circumstances which determine whether the motion of water shall be direct or sinuous, and the law of resistance in parallel channels. *Proceedings of the Royal Society of London*, 35(224-226):84–89, 1883.

[7] O. Reynolds. On the dynamical theory of incompressible viscous fluid and the determination of the criterion. *Philosophical Transactions of the Royal Society of London*, 186:84–89, 1895.

[8] L. Prandtl. Uber flussigkeitsbewegung bei sehr kleiner reibung. *Int. Math. Kongr Heidelberg, Leipzig*, 1904.

[9] L. Prandtl. Report on investigation of developed turbulence. *Technical report, NACA Report*, (TM-1231), 1925.

[10] T.V. Kármán. Mechanische anlichkeit und turbulenz. *Nachrichten von der Gesellschaft der Wissenschaften zu Gottingen, Mathematisch-Physikalische Klasse*, pages 58–76, 1930.

[11] J. Nikuradse. Untersuchungen über die Strömungen des Wassers in konvergenten und divergenten Kanälen. *Forsch. Geb. Ing. Wes*, Heft 289, 1929.

[12] H. Reichardt. Messungen turbulenter Schwankungen. *Naturwissenschaften. Jahrg*, 26(24/25):404, 1938.

[13] H.C.H et al Ng. Comparison of turbulent channel and pipe flows with varying Reynolds number. *Exp Fluids*, 26(24/25):404, 2011.

[14] R.B. Dean. Reynolds number dependence of skin friction and other bulk flow variables in two-dimensional rectangular duct flow. *J. Fluids Eng. Trans. ASME*, 100:215–223, 1978.

[15] G.T. Skinner. *Mean Speed Measurements in Two-Dimensional, Incompressible, Fully-Developed Turbulent Channel Flow.* Thesis.

[16] A.K.M.F. Hussain and W.C. Reynolds. Measurements in Fully Developed Turbulent Channel Flow. *ASME J. Fluids Eng.*, 97:568–580, 1975.

[17] J. Nikuradse. Laws of Flow in Rough Pipes. *Washingon: National Advisory COmmittee for Aeronautics*, 1950.

[18] Antonia R. Raupach, M.R. and S. Rjagopalan. Rough-wall turbulent boundary layers. *Appl. Mech. Rev.*, 44:1–25, 1991.

[19] J. Jiménez. Turbulent flows over rough walls. *Annu. Rev. Fluid Mech.*, 36:173–196, 2004.

[20] H. Schlichting. Experimentelle unterscuchungen zum rauhigkeitsproblem. *Ing-Arch*, 7:1–34, 1936.

[21] A.A. Townsend. *The Structure of Turbulent Shear Flow*. Cambridge University Press.

[22] Sung H.J. Lee, J.H. and P.A. Krogstad. Direct Numerical Simulation of the Turbulent Boundary Layer over a Cube Roughened Wall. *J. Fluid Mech.*, 669:397–431, 2011.

[23] P.-A Krogstad and R. A. Antonia. Surface roughness effects in turbulent boundary layers. *J. Fluid Mech.*, 27:450–460, 1999.

[24] Sung H.J. Lee, S.H. Direct numerical simulation of the turbulent boundary layer over a rod-roughened wall. *J. Fluid Mech.*, 584:125–146, 2007.

[25] Schultz M.P Flack K.A. Volino, R.J. Turbulence structure in boundary layers over periodic two- and three-dimensional roughness. *J. Fluid Mech.*, pages 1–19, 2011.

[26] Schofield W.H. Joubert P. Perry, A.E. Rough wall turbulent boundary layers. *J. Fluid Mech.*, 37:383–413, 1969.

[27] L.F. Jeromin. The status of research in turbulent boundary layers with fluid injection. *Progress in aeronautical sciences*, pages 65–189, 1966.

[28] Moffat R.J. Kays W.M. Healzer, J.M. The turbulent boundary layer on a porous rough plate: experimental heat transfer with uniform blowing. *ASME paper*, pages 74–HT–14, 1974.

[29] Gallaher W.H. Leonard C.A. Dershin, H. Direct measurement of skin friction on a porous flat plate with mass injection. *AIAA J.*, 5:1934–9, 1967.

[30] R.L. Simpson. Characteristics of turbulent boundary layers at low reynolds numbers with and without transpiration. *J. Fluid Mech.*, 42(4):769–802, 1970.

[31] Choi H. Park, J. Effects of uniform blowing or suction from a spanwise slot on a turbulent boundary layer. *Physics of Fluids*, 11.10:3095–3105, 1999.

[32] V. Kornilov. Distribution of mean velocity in turbulent boundary layer over permeable surface with air blowing. *Thermophysics and Aeromechanics*, 19.1:9–16, 2012.

[33] Labraga L. Haddad, M. and L. Keirsbulck. Turbulence structure downstream of a localized injection in a fully developed channel flow. *J. Fluids Eng.*, 128:611–617, 2006.

[34] Kays W.M. Moffat, R.J. The turbulent boundary layer on a porous plate: experimental heat transfer with uniform blowing and suction. *Dept. of Mech. Engrg., Stanford University*, Report No. HMT-1, 1967.

[35] W.M. Kays. Heat transfer to the transpired turbulent boundary layer. *Dept. of Mech. Engrg., Standord University*, Report No. HMT-14, 1971.

[36] J.M. McDonough. *Introductory Lectures on Turbulence.* Dept. of Mech. Engrg., University of Kentucky.

[37] A.J. Reynolds. *Turbulent Flows in Engineering.* John Wiley & Sons.

[38] Bergman R. Harvey J. Duryea G. Holden, M. and J. Moselle. Studies of the structure of attached and separated regions of viscous/inviscid interaction and the effects of combined surface roughness and blowing in high reynolds number

hypersonic flows. *Technical Report CUBRC-88682, Calspan UB Research Center Buffalo NY*, 1988.

[39] J. A. Schetz and B. Nerney. Turbulent boundary layer with injection and surface roughness. *AIAA Journal*, 15.9:1288–1294, 1977.

[40] Yarin A.L. Foss J.F. Tropea, C. *Springer Handbook of Experimental Fluid Mechanics*. Springer.

[41] Blows L.G. Tanner, L.H. A study of the motion of oil films on surfaces in air flow with application to the measurement of skin friction. *J. Phys. E.*, 9:194–202, 1976.

[42] J.H. Preston. The determination of turbulent skin friction by means of Pitot tubes. *J. R. Aeronaut. Soc.*, 58:109–121, 1953.

[43] F.H. Clauser. Turbulent boundary layers in adverse pressure gradients. *J. Aeronaut. Sci.*, 21:91–108, 1954.

[44] K.G. Winter. An outline of the techniques available for the measurement of kin friction in turbulent boundary layers. *Prog. Aerospace Sci.*, 18:1–57, 1977.

[45] B. Estejab. *An investigation of the reynolds number dependence of the nearwall peak in canonical wall bounded turbulent channel flow.* Dept. of Mech. Engrg., University of Kentucky.

[46] Durst F. Zanoun, E. S. and N. H. Evaluating the law of the wall in two-dimensional fully developed turbulent channel flows. *Phys. Fluids*, 15:3079–3089, 2003.

[47] J.P. Monty. *Developments in Smooth Wall Turbulent Duct Flows.* University of Melbourne.

[48] E. Laws and J. Livesey. Flow through screens. *Annu. Rev. Fluid Mech.*, 10:247–266, 1978.

[49] Willert C.E. Wereley S.T. Kompenhans J. Raffel, M. *Particle Image Velocimetry: A Practical Guide.* Springer Science & Business Media.

[50] J. Lachaud and N.N. Mansour. *Validation of a volume-averaged fiber-scale model for the oxidation of a carbon-fiber preform.* Proceedings of the 42nd AIAA Thermophysics Conference.

[51] Wilder M.C. Reda, D.C. and D.K. Prabhu. Trasnsition experiments on slightly blunted cones with distributed roughness in hypersonic flight. *42nd AIAA Thermophysics Conference*, 2011.

[52] Kunkel G.J. Smits A.J. Langelandskvik, L.I. Flow in a commercial steel pipe. *J. Fluid Mech.*, 595:323–339, 2008.

[53] Allen J.J. Smits A.J. Shockling, M.A. Roughness effects in turbulent pipe flow. *J. Fluid Mech.*, 564:267–285, 2006.

[54] Hussain F. Schoppa W. Jeong, J. and J. Kim. Coherent structures near the wall in a turbulent channel flow. *J. Fluid Mech.*, 332:185–214, 1997.

[55] Moin P. Kim, J. and R.D. Moser. Turbulence statistics in fully developed channel flow at low reynolds number. *J. Fluid Mech.*, 177:133–166, 1987.

[56] Moser R.D. Mansour, N.N. and J. Kim. Reynolds number effects in low reynolds number turbulent channels. *Case PCH10 in AGARD*, AR-345:5–8, 1996.

[57] Westerweel J. Adrian, R. *Particle Image Velocimetry.* Cambridge University Press.

[58] K. Hinsch. *Particle Image Velocimetry in Speckle Metrology.* Marcel Dekker Inc.

[59] J. Westerweel. *Digital particle image velocimetry: theory and application*. Delft University Press.

[60] Schultz M.P. Flack, K.A. and T.A. Shapiro. Experimental support for townsends reynolds number similarity hypothesis on rough walls. *Physics of Fluids*, 17:035102, 2005.

[61] Antonia R. Krogstad, P.A. and L. Browne. Comparison between rough and smooth-wall turbulent boundary layers. *J. Fluid Mech.*, 245:599–617, 1992.

[62] A. Mills and X. Huang. On the skin friction coefficient for a fully rough flat plate. *J. Fluid Mech.*, 105:364–365, 1983.

[63] Bergstrom D. Tachie M. Akinlade, O. and L. Castillo. Outer flow scaling of smooth and rough wall turbulent boundary layers. *Experiments in Fluids*, 37:604–612, 2004.

Vita

Jacob Helvey was born in Lexington, Kentucky, the son of Mitchell and Jamie Helvey. After graduating from Lafayette High School, he attended Morehead State University to study physics and play collegiate level baseball. He received his bachelor's of science degree in engineering physics in May of 2011. During the following years, he pursued a master's of science degree in mechanical engineering at the University of Kentucky with a focus in fluid mechanics.